# Data Specifications for Battery Manufacturing Digitalization: Current Status, Challenges, and Opportunities

Franco Zanotto, Diana Zapata Dominguez, Elixabete Ayerbe, Iker Boyano, Christine Burmeister, Marc Duquesnoy, Marlene Eisentraeger, Jonathan Florez Montaño, Alfonso Gallo-Bueno, Lukas Gold, et al.

Batteries & Supercaps

Review
doi.org/10.1002/batt.202200224

Chemistry Europe
European Chemical Societies Publishing

www.batteries-supercaps.org

# Data Specifications for Battery Manufacturing Digitalization: Current Status, Challenges, and Opportunities

Franco M. Zanotto+,[a, b] Diana Zapata Dominguez+,[a, b] Elixabete Ayerbe,[c] Iker Boyano,[c] Christine Burmeister,[d] Marc Duquesnoy,[a, e] Marlene Eisentraeger,[f] Jonathan Florez Montaño,[g] Alfonso Gallo-Bueno,[h] Lukas Gold,[i] Florian Hall,[j] Nicolaj Kaden,[k] Bernhard Muerkens,[l] Laida Otaegui,[h] Yvan Reynier,[m] Simon Stier,[i] Matthias Thomitzek,[n] Artem Turetskyy,[n] Nicolas Vallin,[o] Jacob Wessel,[p] Xukuan Xu,[q] Jeyhun Abbasov,[a, b] and Alejandro A. Franco*[a, b, e, r]

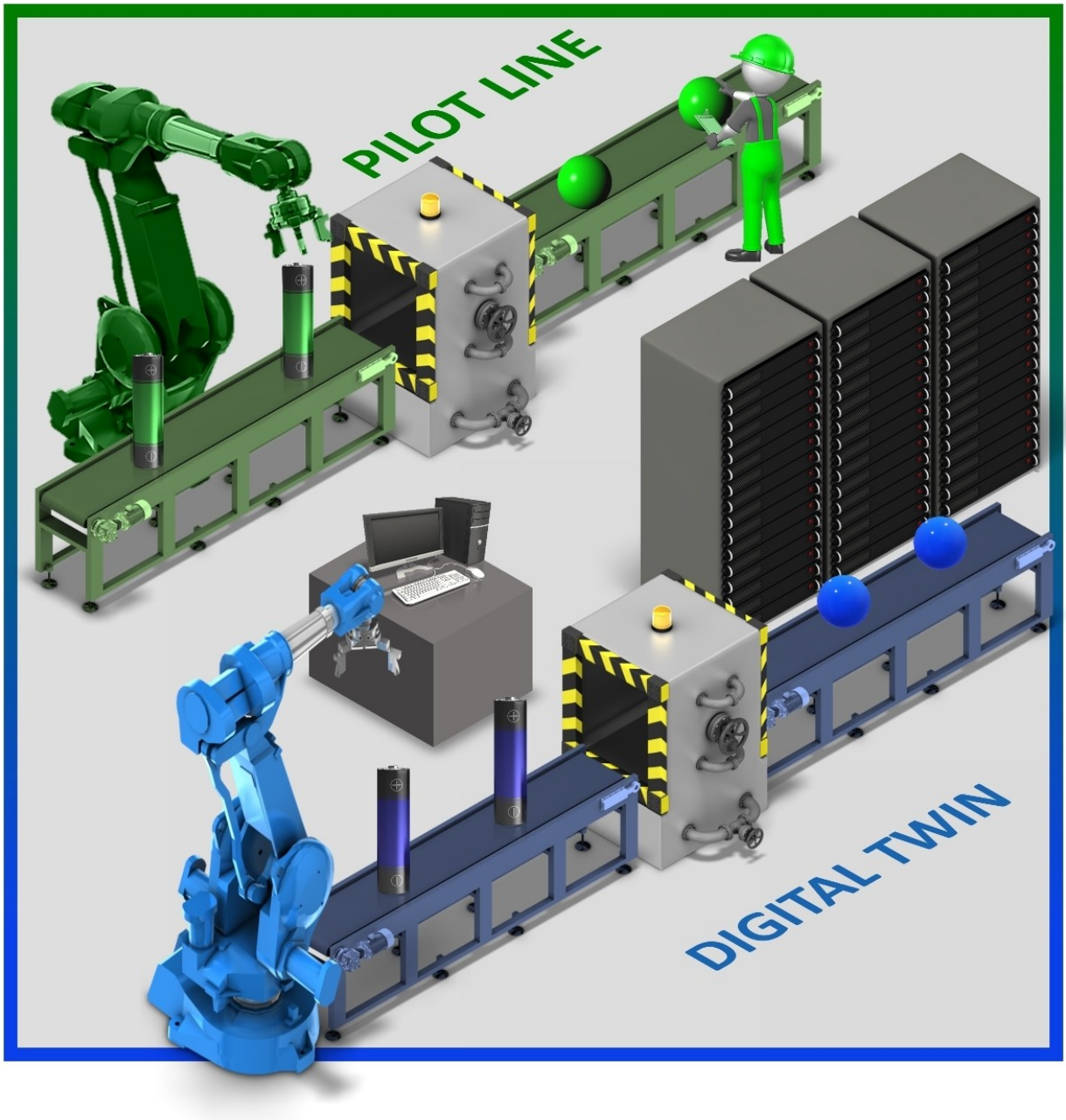

Lithium-ion battery (LIB) manufacturing requires a pilot stage that optimizes its characteristics. However, this process is costly and time-consuming. One way to overcome this is to use a set of computational models that act as a digital twin of the pilot line, exchanging information in real-time that can be compared with measurements to correct parameters. Here we discuss the parameters involved in each step of LIB manufacturing, show available computational modeling approaches, and discuss details about practical implementation in terms of software. Then, we analyze these parameters regarding their criticality for modeling set-up and validation, measurement accuracy, and rapidity. Presenting this in an understandable format allows identifying missing aspects, remaining challenges, and opportunities for the emergence of pilot lines integrating digital twins. Finally, we present the challenges of managing the data produced by these models. As a snapshot of the state-of-the-art, this work is an initial step towards digitalizing battery manufacturing pilot lines, paving the way toward autonomous optimization.

## 1. Introduction

Energy storage is one of the most important challenges humanity needs to face in the XXI century.[1] This challenge is triggered by the depletion of fossil energy sources, climate change, and the consequent massive use of intermittent renewable energies and electrification of the transportation sector. Within this context, lithium-ion batteries (LIBs) are being called to play a central role. The needed massive deployment of LIBs, in particular, to satisfy the demand from the electric vehicle (EV) sector, pushes battery manufacturers to multiply the number of Gigafactories to reduce the cost of production.[2,3] Many of these Gigafactories will be built in Europe, which is expected to become the second-largest producer of LIBs after China by 2025.[4] These cost-driven large-scale production efforts are accompanied by efforts to further optimize LIBs in terms of performance, durability, safety, recyclability, sustainability, and manufacturing $CO_2$ fingerprint. The latter efforts are carried out at the prototyping level, which is a critical and intermediate step between the level where materials are being developed and industrial production. The prototype level is where an early approximation of the final LIB cell product is manufactured, tested, and reworked. This is done until LIB cells with desired characteristics (e.g., performance) are manufacturable. Prototyping is needed as all the details and requirements to make materials work in full cells are not known well in advance. This is then a trial-and-error process that works in an iterative way. As the manufacturing process of LIBs involves multiple steps which are sequentially

[a] *Dr. F. M. Zanotto,[+] Dr. D. Z. Dominguez,[+] M. Duquesnoy, J. Abbasov, Prof. Dr. A. A. Franco*
*Laboratoire de Réactivité et Chimie des Solides (LRCS), UMR CNRS 7314*
*Université de Picardie Jules Verne, Hub de l'Energie*
*15, rue Baudelocque, 80039 Amiens Cedex, France*
*E-mail: alejandro.franco@u-picardie.fr*
[b] *Dr. F. M. Zanotto,[+] Dr. D. Z. Dominguez,[+] J. Abbasov, Prof. Dr. A. A. Franco*
*Réseau sur le Stockage Electrochimique de l'Energie (RS2E), FR CNRS 3459, Hub de l'Energie*
*15, rue Baudelocque, 80039 Amiens Cedex, France*
[c] *E. Ayerbe, Dr. I. Boyano*
*CIDETEC, Basque Research and Technology Alliance (BRTA)*
*P° Miramón 196, 20014 Donostia – San Sebastian, Spain*
[d] *Dr. Ing. C. Burmeister*
*Institute for Particle Technology, Technische Universität Braunschweig*
*Volkmaroder Straße 5, 38106 Braunschweig, Germany*
[e] *M. Duquesnoy, Prof. Dr. A. A. Franco*
*Alistore-ERI European Research Institute*
*CNRS FR 3104, Hub de l'Energie, 80039 Amiens, France*
[f] *M. Eisentraeger*
*Bereich Gesellschaft und Innovation/Department Society and Innovation*
*VDI/VDE Innovation + Technik GmbH*
*Steinplatz 1, 10623 Berlin, Germany*
[g] *Dr. Ing. J. F. Montaño*
*University of Applied Sciences Landshut, Technology Center for Energy*
*Wiesenweg 1, 94099 Landshut Ruhstorf, Germany*
[h] *Dr. A. Gallo-Bueno, Dr. L. Otaegui*
*Centre for Cooperative Research on Alternative Energies (CIC energiGUNE)*
*Basque Research and Technology Alliance (BRTA), Alava Technology Park*
*Albert Einstein 48, 01510 Vitoria – Gasteiz, Spain*
[i] *L. Gold, S. Stier*
*Fraunhofer Institute for Silicate Research ISC*
*Neunerplatz 2, 97082 Würzburg, Germany*
[j] *F. Hall*
*Leclanché GmbH*
*Industriestrasse 1, 77731 Willstätt, Germany*
[k] *N. Kaden*
*Institute of Machine Tools and Production Technology (IWF),*
*Production Technologies & Process Automation,*
*Technische Universität Braunschweig*
*Langer Kamp 19b, 38106 Braunschweig, Germany*
[l] *B. Muerkens*
*YXLON International GmbH*
*Essener Bogen 15, 22419 Hamburg, Germany*
[m] *Dr. Y. Reynier*
*Université Grenoble Alpes*
*CEA LITEN, F-38054 Grenoble, France*
[n] *M. Thomitzek, A. Turetskyy*
*Institute of Machine Tools and Production Technology (IWF),*
*Sustainable Manufacturing and Life Cycle Engineering,*
*Technische Universität Braunschweig*
*Langer Kamp 19b, 38106 Braunschweig, Germany*
[o] *N. Vallin*
*Dassault Systèmes SE*
*10 Rue Marcel Dassault, 78140 Vélizy – Villacoublay, France*
[p] *J. Wessel*
*Institute of Machine Tools and Production Technology*
*Langer Kamp 8, 38106 Braunschweig, Germany*
[q] *X. Xu*
*Aschaffenburg University of Applied Sciences*
*Würzburger Str. 45, 63743 Aschaffenburg, Germany*
[r] *Prof. Dr. A. A. Franco*
*Institut Universitaire de France*
*103 boulevard Saint Michel, 75005 Paris, France*
[+] *These authors contributed equally to this work.*

coupled and include numerous parameters, the optimization of LIB cell prototypes is a time-consuming and costly process.

Approaches based on the design of experiments are currently used to ease such an optimization, but they are recognized not to be enough to deal in an efficient way with the underlying complexity of the traditional LIB manufacturing processes.[5,6] Scrap rates, especially from battery companies, are difficult to assess, but we estimate that they can be as high as 30% for battery prototyping, a number not far away from previous estimations.[7] Computational physical modeling supported by mathematical descriptions of these processes as well as the blooming artificial intelligence (AI) and machine learning (ML) techniques give the promise to ease the emergence of more efficient approaches able to accelerate LIB prototyping optimization.[8] One of these approaches is the digital twin, a digital «copy» of the real manufacturing process based on physical and AI/ML models.[9]

In state-of-the-art, there is a lack of publications providing a global overview of the links between experimental data and the computational modeling approaches depending on their types.[10] Having a clear and global view of these links is crucial for the emergence of the digital twins of battery manufacturing. Such digital twins, supposed to run in real-time and exchange information with the real prototyping lines as schematized in Figure 1, are constituted at their core by mechanistic or ML models or a combination of both. As this „digital-real» data exchange is supposed to happen in as real-time as possible, it is also important to discuss the available acquisition techniques of experimental data in terms of their accuracy and rapidity in performing the data acquisitions.

The present article is written within the context of the LiPLANET network, a large-scale European initiative aiming to build a more competitive LIB cell manufacturing ecosystem.[11] This network was founded under the European Union's Horizon 2020 Research and Innovation Programme (Grant Agreement No. 875479). The LiPLANET network brings together the most relevant European lithium battery cell pilot lines and key stakeholders to build a more competitive battery cell manufacturing ecosystem and increase production to an industrial scale. Within this ecosystem, research pilot lines for LIB cell production bring together expertise in battery cell and production technology and constitute a crucial infrastructure resource for testing and development of Lithium-based Batteries as well as for the training and education of staff in battery cell manufacturing. Cooperation, as well as the mutual exchange of data, expertise, and access rights between these pilot lines, is crucial to achieving the goal of LiPLANET: by 2030, the network's vision is to be the one-stop-shop service provider for education, knowledge transfer, testing, certification, and pilot-scale production of lithium and post-lithium battery cell technologies for research, industry, and authorities.

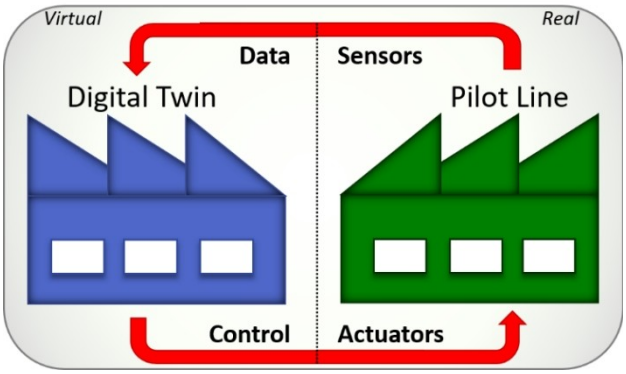


**Figure 1.** Schematic representation of the feedback between the pilot line and its digital twin. Adapted from Ref. [9]. Copyright (2022) The Authors. Advanced Energy Materials published by Wiley-VCH GmbH.

The scope of this article is to cover LIB prototyping aspects, from the materials to the formation step. This article is organized as follows. First, we discuss the parameters involved in battery manufacturing and their interlinks. Second, we discuss different available computational modeling approaches by providing some examples from ongoing projects at the EU level. The goal here is not to be exhaustive but instead to provide a comprehensive overview of the modeling working principles. Then we discuss their practical implementation (software, programming languages). Then, we perform a comprehensive analysis of the different parameters implicated in each manufacturing step regarding their criticality for modeling set-up and validation, measurability, measurement accuracy, and rapidity. This analysis takes the form of tables with color codes that can be seen as metadata schemes for battery manufacturing. In such a way, we identify the missing aspects, remaining challenges, and opportunities for the emergence of pilot lines integrating digital twins. We envisage this set of tables as guidelines for the future development of models and characterization techniques that can be applied online. As they are based on the state-of-the-art, they are bound to become obsolete in their current state. For this reason, we propose to present them online in a readable format. This allows us to update them as models evolve and

Alejandro A. Franco is Full Professor at the Université de Picardie Jules Verne (Amiens, France) and Honorary Member of the Institut Universitaire de France. He is the leader of the Theory Open Platform at the ALISTORE European Research Institute. His research interests encompass multiscale modeling and artificial intelligence applied to batteries for their accelerated design and optimization. He is grantee of an ERC consolidator grant for his project ARTISTIC on the development of a digital twin of battery manufacturing processes. He is the Chairman of the Expert Group "Digitalization, Measurement Methods and Quality" in the European LiPLANET Battery Manufacturing Network.

new characterization techniques become available. For online access to these interactive tables, the reader can go to: https://www.erc-artistic.eu/fileadmin/user_upload/LiPLANET/index.html. A list of acronyms and their corresponding meanings is presented in Table 1 to facilitate the reading of our article.

## 2. State-of-the-Art Manufacturing Process

Pilot-scale LIB cell production is critical for further optimizing manufacturing parameters and cell designs to ensure the smooth transition from lab to industrial scale. Figure 2 introduces the current state-of-the-art LIB cell manufacturing process, which includes three major parts: electrode preparation, cell assembly, and conditioning step (formation and testing).

**Table 1.** List of acronyms used throughout this work.

| Acronym | Meaning | Acronym | Meaning |
|---|---|---|---|
| AI | Artificial Intelligence | LIB | Lithium-ion Battery |
| AM | Active Material | MD | Molecular Dynamics |
| BVCO | Battery Value Chain Ontology | ML | Machine Learning |
| CBD | Carbon-Binder Domain | MP | Machine Parameter |
| CFD | Computational Fluid Dynamics | NDT | Non-Destructive Test |
| CGMD | Coarse-Grained Molecular Dynamics | NMP | N-methyl-2-pyrrolidone |
| CMC | Carboxymethyl Cellulose | PP | Process Parameter |
| CT | Computed Tomography | PSD | Particle Size Distribution |
| CV | Computer Vision | PSO | Particle Swarm Optimization |
| DEM | Discrete Element Method | RVE | Representative Volume Element |
| EV | Electric Vehicle | SD | Stochastic Dynamics |
| FEA | Finite Element Analysis | SEI | Solid Electrolyte Interface |
| FEM | Finite Element Method | SIB | Sodium Ion Batteries |
| FF | Force Fields | SoC | State of Charge |
| FMEA | Failure Mode and Effects Analysis | SoH | State of Health |
| GPO | General Process Ontology | SP | Structure Parameter |
| LBM | Lattice Boltzmann Method | TBS | Technical Building Services |

First, the mixing step is carried out where the active material (AM), conductive additive, and binder are mixed to form a uniform slurry with the solvent.[12] Currently, electrodes can be prepared using either water or N-methyl-2-pyrrolidone (NMP) as a solvent. Although NMP is more commonly used, in recent years, there has been great progress in the development of water-based electrodes, which are suitable for sustainable production.[13,14] The current pilot lines employ planetary mixers to prepare large-volume slurries for production and transition to continuous and thus more efficient extrusion processes.[15,16] The electrochemical performance of the electrodes is also highly related to the mixing condition and operation, as the mixing uniformity can affect the electrode microstructure and materials distribution.[17]

Current coating lines in the pilot-scale consist of three main parts: slurry application on the substrate (current collector), several drying units, and slitting/rewinding of the processed laminates. The thickness of the coated electrodes determines, among other factors such as specifications and composition, the electrodes' areal capacity and, further, current capability, the viscosity of the electrode slurry plays a crucial role and is therefore monitored and controlled before obtaining a high-quality, homogeneous coating. Especially for thicker electrodes, binder migration to the upper side of the coating is a major challenge in this particular step. It impacts not only to mechanical adherence of the coating to the current collector (adhesive strength) but also between AM particles (cohesive strength), compromising electrochemical performance due to the blocking of the electrodes near the separator.[18–20]

Among other important parameters of the electrodes' properties, the porosity, pore size distribution, and tortuosity factor are crucial for final cell performance. The porosity, for instance, is chosen accordingly, ensuring good contact

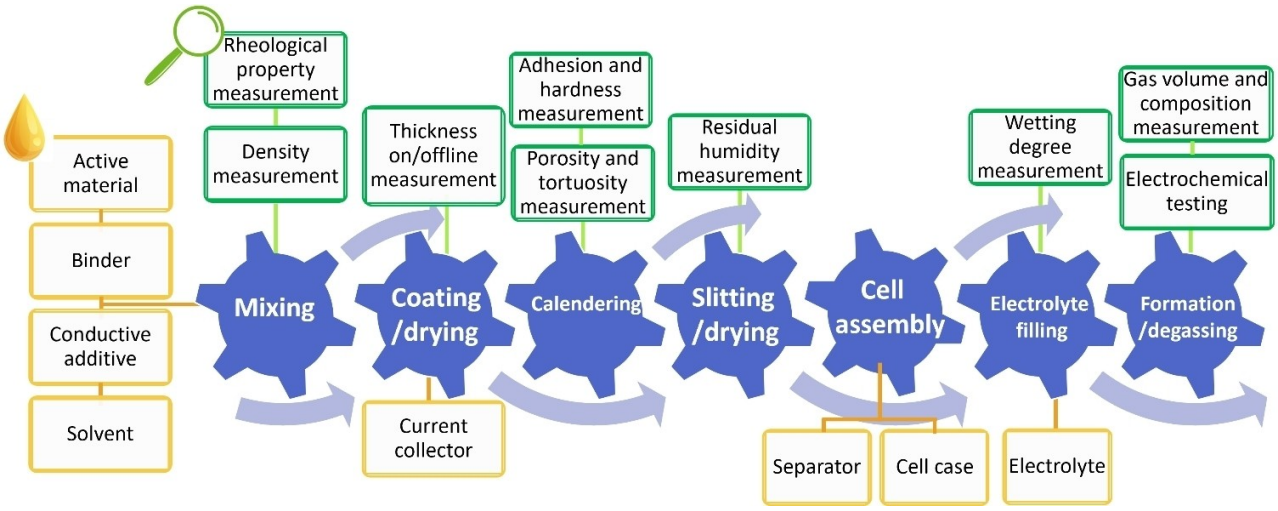


**Figure 2.** Schematic of the LIB manufacturing process, detailing its main steps (purple), their corresponding necessary elements (yellow), and the control measurements (green).

between the particles, electrolyte wetting, and defined energy and power density. Currently, the electrodes are compacted by a two-roll smoothing calender under high pressure and evaluated temperatures increasing contact between the coating and the current collector and reducing the electrode porosity, resulting in an increase in the fast-charging capability with an improvement of the cell's lifespan.

The final contours of anode and cathode sheets are mechanically punched in the conventional manufacturing plants. Laser cutting is a suitable approach to replace current technology as mechanical punching is associated with tool wear and inflexibility in the cell and electrode design.[21] Particles produced by laser cutting are extracted to avoid interaction with the incident laser beam and significantly reduce the number of particles on the final electrode surfaces and the kerf. These contaminations and laser-induced material modifications could be starting points for chemical degradation or lithium plating, affecting the battery cells' overall performance.

Both electrodes are (z)-stacked (for pouch cells, wound for other types) in parallel, divided by the separator, and placed into the foil pouch. The cell stacking is conventionally performed in a dry room under elevated conditions and a dew point of about −60 °C, depending on the chemistry and handled materials. Important factors in the cell stacking process include positioning accuracy and processing speed. Other approaches include the lamination of the separator with the electrodes, leading to lower cell scrap rates related to short-circuit and increasing stacking/winding rates.

Accelerated and homogenized electrolyte wetting has a significant impact on cycle lifetime. The objective of the electrolyte filling step is to optimize the protocol to avoid spontaneous cell failure and to increase cycle lifetime by a factor of two or more.

The cell conditioning step (formation and testing) is another element in the LIB manufacturing picture. This step takes several days, if not weeks, and a considerable portion of the production plant space. This final step ensures that the inner components (electrodes and separator sheets) are properly wetted with the electrolyte. A stable Solid-Electrolyte Interface (SEI) layer is formed on the anode's side. In addition, it is useful for final failure detection and discard of such cells. Several approaches are currently under investigation to improve the formation and testing procedure. Most of the concepts aim to improve SEI layer growth via either (1) changing the cycling protocol itself,[22,23] (2) precoating the particles, or (3) the addition of different electrolyte additives.

## 3. Computational Modeling

### 3.1. Overall battery modeling landscape

Computational methodologies innovation is following the LIBs development. Over the past years, there has been significant improvement in the ability to develop computational physics-based models that describe the complexity of LIBs.[24] The multiphysics characteristics of these devices make the task challenging, first to cover all the physics and second, to couple them. Particular challenges arise in developing models that deal in a deterministic way with the various scales of LIB components, from the atomistic to the macroscale level.[25] While some academic groups remain specialized in models accounting for one or few physics and scales, others develop the capability to build coupled multiphysics models. Many works have been reported on modeling materials, electrochemistry, transport processes, thermal management, and mechanics in LIBs. Software vendors have been building software solutions based on the computational physics-based methodologies reported by academic groups, which still lead to innovation in the field. Indeed, there is still some work to do for commercial software because validation of the models requires exposure to field data, which is sometimes difficult to find with the right amount and the right quality in the literature, or industrial cell manufacturers due to IP protection. Furthermore, AI/ML is increasingly used in the LIB field for multiple purposes, such as materials discovery, cell aging prediction, or surrogate modeling.[8,26,27]

Overall, the scope of computational modeling goes beyond materials or cell engineering, with increased attention to the LIB manufacturing process, as discussed in the following.

### 3.2. Approaches for battery manufacturing simulations

Following the trend of LIB modeling discussed above, computational tools for simulating LIB manufacturing/production processes are either physics-based (hereafter called *mechanistic*) or data-based methods. The two model paradigms differ fundamentally in their approaches. While mechanistic modeling describes the causal physical-chemical cause-effect relationships in the processes and the product, data-based modeling maps the correlation of various parameters within the recorded data. The mechanic models are usually valid over a wide range of observations since the underlying system behavior is described, but they require enormous computation times. On the other hand, the data-based models may not be extrapolated over the data space under consideration but can be solved very quickly.

In order to describe not only single processes but the entire process chain, different process models must be combined via defined intersections. The intersections are the structural parameters of the intermediate product in the respective process steps. These structural parameters are either inherent to the material (density of the AM) or can be altered (coating thickness during calendering), or created (porosity during drying) along the process chain.

The process characteristics predetermine the modeling paradigm utilized for each process. Overall, many different modeling approaches have been successfully applied to describe the process-product interaction, e.g., Coarse-Grained Molecular Dynamics (CGMD), Discrete Element Method (DEM), Computational Fluid Dynamics (CFD), or analytic models. Combining different process models, which are typically solved

in specialized software environments, can cause significant challenges regarding the compatibility of the modeling paradigm or the accumulation of computation times.

In the following, we provide some concrete examples of mechanistic and data-driven models' achievements (described broadly in Table 2). We do not intend to be exhaustive here, as the computational modeling of LIB manufacturing has already been reviewed recently.[8,9,24] Instead, we want to provide practical details of how some of the recently reported approaches are implemented and which types of experimental parameters they require. For this purpose, we pick mostly examples of ongoing projects in Europe: ARTISTIC (funded by the European Research Council), DEFACTO (funded by the Horizon 2020 program), and Sim4Pro (funded by the German Federal Ministry of Education and Research).

ARTISTIC is a project started in 2018 aiming to develop a digital twin of the entire manufacturing process of LIBs: mixing, slurry coating, drying, calendering, electrolyte filling, formation, and resulting electrochemical performance. The approach encompasses mechanistic and data-driven models sequentially coupled, e.g., the outputs of the drying model go as inputs of the calendering model, etc. The former describes the physics with 3D spatial resolution as a function of time. It predicts the impact of manufacturing parameters (e.g., slurry formulation, drying rate, calendering pressure) on the 3D-electrode architecture at the mesoscale and associated electrochemical performance. The data-driven models are used to accelerate the mechanic model's parameterization, treat pilot line experimental data, and derive surrogate versions of the mechanic models. The latter allows deriving optimization loops to inverse designing LIB manufacturing, i.e., predicting the manufacturing parameters to adopt to maximize/minimize multiple properties of LIB electrodes. The ARTISTIC project has recently delivered an online calculator that can be used from any Internet Browser. Thanks to a user-friendly graphical interface, users can launch slurry, drying, and calendering simulations, with more functionalities to be added soon.[28] The users can also explore the databases produced in the project and download the 3D-resolved electrode mesostructures and corresponding properties (e.g., electrode slurry density value, electrode porosity value) for their own research. The ARTISTIC project has also demonstrated the chemistry neutrality of the adopted computational approach, which can deal with electrode manufacturing based on both commercial and *in-house*-elaborated AMs for LIBs and Sodium-Ion Batteries (SIBs), respectively.[29]

Similarly to ARTISTIC, the Sim4Pro project, started in 2019, aims to establish a digitization platform that addresses the high complexity of battery cell production by considering the influence of individual production steps on the structure of intermediate and final products to predetermine the performance of a battery cell. The used modeling framework links the models of the process chain with battery cell simulations. The process models describe the relationship between the process and the resulting structure for each process step (e.g., mixing, coating, calendering). They include both analytical models based on mass or energy balances and numerical models (using CFD or DEM). The process models are connected via structural (output) parameters like mass loading, coating density, and electrode composition, employed as input parameters to characterize structure-performance relationships by battery simulations. Based on the results of the individual process models, empirical meta-models are developed. This enables the generation of simulation results in real time. Eventually, the connection enables an *in silico* analysis of process-product interactions. The modeling framework considers nominal values and parameter uncertainties caused by the machine and material imprecisions propagating along the process chain, resulting in uncertain battery cell properties. The results are utilized for robust optimization, uncertainty sensitivity analysis, and identification of production tolerances, form the basis for process cost and process resource efficiency functions, and allow for a comprehensive ecological and economic evaluation.

The H2020 project "DEFACTO" aims at contributing to the increase in the competitiveness of the European battery cell manufacturing industry by developing multiphysics models for the LIBs manufacturing main steps, such as the ones that mimic the behavior of the electrode drying and calendering steps, as well as the electrolyte filling step. In addition, a multi-scale multiphysics workflow is conducted to gain in-depth insight into the mechanical aspects of the cell's components, their corresponding degradation mechanisms, and the crosslink with the manufacturing parameters. The resulting simulation tools will predict optimized cell design and cell manufacturing parameters validated by prototyping and manufacturing data of advanced generation 3b cells, from current industrial cells to next-generation 3b prototype cells. In addition, multi-scale characterization tests will also be conducted to provide data for model development and validation and to understand manufacturing process parameters and cell aging mechanisms. Finally, the project aims to also contribute to the current battery standardization landscape.

**Table 2.** Main characteristics of data-driven and mechanistic modeling.

| Data-driven models | Mechanistic models |
|---|---|
| Based on experimental data of the system | Based on assumptions about the mechanisms of the system |
| Input parameters frequently do not have a physical meaning | Parameters generally have a mechanical or physiological meaning |
| The number of parameters is not predetermined by the system | The number of parameters in the model is fixed |
| Fitting of input-output behavior from measured data, e.g., polynomials, Artificial Neural Networks, support vector regression | Described by balance equations of conserved quantities which change in time and space (algebraic equations, Ordinary Differential Equations, Partial Differential Equations) |
| Show correlation possibly without causation | Show causation based on mechanistic relations |
| Model results are limited to the space of their calibration; extrapolation is not suitable | Aim to represent system knowledge and thus show higher extrapolation power |
| Require large amounts of data | Require very small amounts of data |
| Running requires low computational cost | Running requires a high computational cost |

### *3.2.1. Slurry and coating modeling*

In the ARTISTIC project, the electrode slurry is simulated in 3D using the CGMD approach by using the software LIGGGHTS.[30] Classical Newton equations are numerically solved using the LAMMPS software in this approach. These equations describe the relationship between the interaction forces (or force fields – FFs–) between the particles in the slurry and their acceleration. The numerical integration of these equations allows calculating the speed and the position evolution of the particles. The interaction forces have been modeled using Lennard-Jones and Granular-Hertzian FFs. These FFs allow capturing the impact of the distance between the particles and their effective radius on the interaction forces magnitude. Two types of particles are considered: the AM and carbon-binder domain (CBD) particles, which are coarse grain carbon additives, binder, and solvent. The inputs of this approach are the AM particle size distribution, the formulation (weight percentages of AM and carbon-binder), and the solid content. The size of the CBD particles is determined as a function of the carbon-binder ratio and the experimental density of the slurry. The simulation procedure starts by randomly placing the AM and CBD particles in a box in periodic boundary conditions (Figure 3a). Then the MD is run until the system converges to an equilibrium state (Figure 3b). This state corresponds to the partial overlap between the CBD particles and the CBD and the AM particles. The corresponding 3D mesostructure depends on the FFs parameter values and the assumed size for the CBD particles. Therefore, this approach requires fitting these parameter values. This is performed by fitting the calculated slurry density and the calculated viscosity *vs.* share-rate curve to the experimental ones. The latter is calculated using Non-Equilibrium MD simulations, where the mesostructured slurry box is deformed at different shear rates (Figure 3c). The model can very well reproduce the shear-thinning behavior for different formulations and solid contents. The fitting procedure of the FF parameter values can be carried out manually or automatically. Obviously, the second option is prioritized in the project. We have demonstrated that automatized methods decrease computational cost by a factor of 20. Automatized methods developed in the project include Particle Swarm Optimization (PSO), ML, and a combination of both. In short, PSO is a stochastic global optimization algorithm based on swarm behavior, which tries to iteratively improve a candidate solution regarding a given measure of quality defined as the difference between the calculated slurry viscosities and densities of the experimental ones. Furthermore, ML is also used to predict the viscosity calculation result from the first numerical steps of a non-equilibrium MD simulation: This allows for performing the fitting process in a faster way as each CGMD model has a different set of FFs parameters values, and it is used in optimization algorithms that do not need to run until the end.[31] The ARTISTIC project demonstrated this slurry modeling approach for multiple AM chemistries, such as NMC111, LFP, graphite, and organic AM for SIBs.[30–32]

ML has also been applied in the ARTISTIC project for the prediction of the impact of slurry formulation, solid content, and viscosity (determined by the coater comma-gap and coating speed) on the loading and porosity of the fabricated electrodes (the drying rate kept constant).[33] For this purpose, an experimental data set (*ca.* 80 experimental conditions, each of them repeated five times) was collected in order to predefine several classes (low, medium, high) based on experimental knowledge from loading and porosity values. The resulting dataset was divided into a training and testing dataset, whose main goal was to train a supervised classification model (Support Vector Machine) to fit those classes as a function of input variables (formulation, solid content, viscosity). The resulting trained model allowed to assess interdependencies between the levels of electrode properties and the manufacturing parameters through a straightforward graphical representation, with a trustable accuracy (above 80%) from an experimental point of view. The ML approach was compared with different supervised algorithms, such as Decision Tree and Deep Neural Network. The latter analogy enabled to analyze

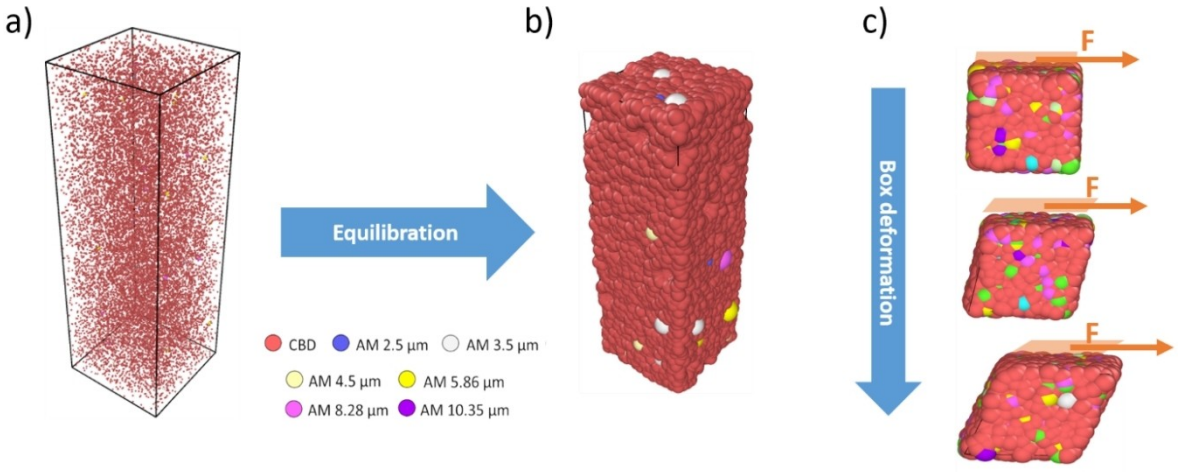


**Figure 3.** Slurry model steps within the ARTISTIC model. a) Randomly generated initial positions. b) Slurry structure after equilibration. c) box deformation performed at a constant shear rate for the calculation and fitting of viscosity curves. Adapted from Ref. [30]. Copyright (2020) The Authors. Published by Wiley-VCH Verlag GmbH & Co. KGaA.

the evolution of predictive capabilities regarding the type of algorithm applied for the training/testing, allowing to see which approach was the most meaningful for assessing the trends between electrode properties and its manufacturing parameters. Complementary experimental characterizations of the viscoelastic slurry behavior supported the results, connecting the conclusions with chemistry-based interpretations.

Coating modeling is closely related to slurry modeling. Ding *et al.* have reviewed several theoretical models for coating.[34] The coating bead is stable within certain parameter ranges, and the coated layer remains defect-free. Here the parameter ranges are set by capillary pressure in the coating bead, and a capillary model can be used.[35] If surface tension effects can be ignored, the parameter ranges are set by viscous pressure, and defects such as air bubbles, periodic thickness variations, and dripping can occur; a viscous model applies here.[36] Numerical studies based on CFD can give more detail on the flow field within the coating bead. Carvalho and coworkers have developed a series of 2D models to study slot coating. The first one allowed them to predict the parameter ranges needed to obtain a defect-free coated layer,[37] a second one explored the lower limits for layer thickness,[37] and a third one extended this model to mildly viscoelastic fluids,[38] all relevant to the electrode slurries.

In general, a post-treatment on electrode properties enables to go beyond common analysis with manual tunings by automatically assessing the labeling of experimental datasets for better manufacturing knowledge. The ARTISTIC project demonstrated the approach by defining heterogeneous electrodes from a batch of experimental measurements from NMC-622 coated electrodes after varying the most critical fabrication parameters from the slurry and coating steps. This involves an evaluation of new electrode characteristics without any prior manual labeling, whose main goal is to identify the most relevant properties for heterogeneous electrode definition. This step was done according to a dimensionality reduction of the dataset and a segmentation approach to identify groups of electrodes with similarities in terms of prior and newly defined electrode characteristics. The combination with statistical inference concluded the effect of the associated manufacturing parameters on such heterogeneity, thus giving new perspectives for designing better batteries. In our study case, we took advantage of thickness and mass loading measurements to evaluate different types of heterogeneous electrodes.[39] Similar to this approach, Drakopoulos *et al.*[40] presented a limited dataset including 27 different formulations, manufacturing protocols, and performance properties. They are used to predict and design the formulation and manufacturing process to produce thick, high-coat-weight, graphite-based electrodes.

An important part of the slurry mixing process is the dispersion of carbon-based conductive additives like carbon black to structure the particles and tailor the size distribution to the required function within the electrode network. The CB particle size correlates with the microstructural properties and thus directly affects the cell performance, so optimized processes allow for obtaining adjusted particle size distributions. While the adjustment of machine parameters is often empirical, the comprehension of the process conditions itself by measurements may not be possible but accessible via simulations. The investigation of the dispersion process requires using a multi-scale approach to account for various influences on different length scales.

The fragmentation of carbon black, so the size reduction of agglomerates down to aggregates, is being investigated via the coupling of CFD (coded in the software OpenFoam) with DEM (coded in the software LIGGGHTS) within the project DEFACTO. Each agglomerate consists of several aggregates which are generated randomly, but with defined strength, a number of primary particles, and fractal dimension and are joined together via inter-particular forces, namely van der Waals forces. These forces are stronger within the aggregates than for the bindings to each other.

Then, the effect of size and fractal dimension of single agglomerates within a Representative Volume Element (RVE) with periodic boundaries on the orientation within the shear flow and the resulting shear forces can be described. The shear behavior and the strength of the inter-particular forces determine the breakage of agglomerates so that the number and size of fragments over time and the forces acting on the particulate structures are determined. However, as these studies are costly and mostly limited to very few single agglomerates, they are mainly used to investigate the relation between local shear stress and breakage behavior. Thus, the distributions of shear rate, shear stress, or other dispersion-relevant parameters in the mixing device are determined using CFD simulations. The CFD models (coded in the software OpenFoam) without coupling do not explicitly solve the breakage of CB agglomerates. Still, they consider the shear field in the mixer (e.g., dissolver, planetary mixer, or twin-screw extruder) of the fluid to extract the relevant parameters of stress. Characteristic values are the intensity and number of stresses calculated from the distributions of shear stress and shear rate by using Rumpf's model,[41] and compared to the particular strength agglomerates to estimate their breakage. Finally, the resulting particle size and the specific energy demand are obtained. However, deagglomeration and aggregate breakage are connected to the viscosity and the residence time distribution. Thus, measurements of the residence time distribution and viscosity are required, or an extension of a viscosity model shall be added. This approach is utilized to optimize the machine parameters to obtain the desired size or scale and transfer processes to larger or more complex equipment, e.g., from a batch-operated planetary mixer to a continuous extruder. Extruders allow various screw configurations (consisting of different elements, e.g., conveying elements, kneading blocks, or elements for distributive mixing), which can be seen as a cascade of subsequent mixers, applying different stressing conditions along the screw. As the CFD treats every element separately, using the output data of the preceded screw element as input for the next, the model can account for individual screw combinations and gives a much more detailed insight than merely data-driven models. The physical modeling provides the boundary conditions for data-driven models and thus reduces the amount of data required.

Additionally, population balance models developed for highly filled nanoparticle suspensions can describe the carbon black particle size distribution correlated with the dispersion process resulting from fragmentation. It can be adapted to the required mixing device, e.g., planetary mixers for battery slurries. Due to the high shear rate of the agitator, this type of model assumes that every particle passes the stress zone with sufficient dispersion time. A laminar flow profile for the planetary mixer is approximated, and the stressing intensity dissipated to the carbon black particles is described by the equation of Rumpf. The model considers the conditions within the mixer by a shear rate distribution and accounts for the dependence of the viscosity on particle size distribution and temperature. Additionally, the breakage behavior of the particles under stress is considered by a particle strength function and a breakage function that describes the daughter particle size distribution received by successful dispersion. The population balance model delivers the particle size distribution over the dispersion time as output.

#### *3.2.2. Drying modeling*

Slurry 3D simulations need to be performed as the drying model aims to predict the impact of drying conditions on the 3D-electrode mesostructured. The ARTISTIC project simulates the slurry drying process using the CGMD approach.[42–45] The corresponding drying model takes as an input the slurry mesostructured predicted by CGMD as a function of formulation and solid content. As such, many of the simulation parameters are obtained from this output as well. This includes CBD particle sizes and some of the FF parameters.

Two sub-approaches have been undertaken in this regard. The first one assumes homogeneous drying. This consists of shrinking the CBD volume by some factor to mimic the solvent evaporation, starting from the slurry mesostructured (Figure 4a). This is performed suddenly, and then an MD simulation is run to equilibrate the system again. The resulting mesostructure corresponds to the dried electrode. The CBD shrinking factor has been tuned to reach dried electrode porosities in agreement with the experimental ones. The accounted FFs for the drying simulation are Lennard-Jones and Granular-Hertzian, similarly to the slurry calculations.

The second sub-approach assumes heterogeneous drying (Figure 4b). This sub-approach allows accounting explicitly for the carbon-binder migration. It is built in a way that allows modulating the transition from the slurry to the electrode state as a function of the depth in the slurry. It assumes a faster transition at the top with respect to the bottom of the slurry. This is achieved by dividing the depth of the slurry into several

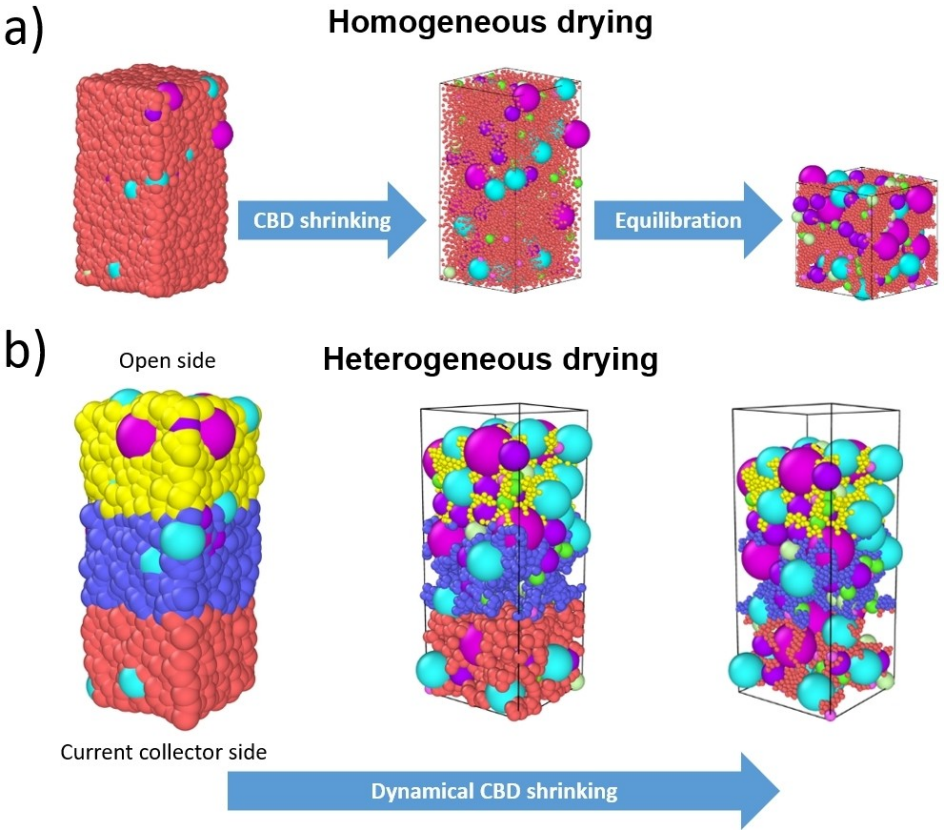


**Figure 4.** The two approaches for modeling the drying step according to the ARTISTIC project. a) Homogeneous drying takes place in two stages: first, a rapid decrease in the size of the CBD particles occurs to account for solvent evaporation, followed by an equilibration step. b) CBD shrinks continuously as the electrode dries and settles in the heterogeneous approach. Different shrinking rates are assigned to different layers to account for fast drying effects. Reproduced with permission from Ref. [45]. Copyright (2021) Elsevier.

zones, and for each of them, the CBD particles shrink at different rates (faster on the top, slower at the bottom). These rates are implicitly related to experimental parameters such as temperature and air flow, though no explicit connection is accounted for. The ratio between the CBD shrinkage rates at the different zones is correlated to the drying rate. This approach allows us to find that: the higher the drying rate, the higher will be the fraction of CBD on the top region in the dried electrode versus the CBD fractions in the middle and the bottom regions; the CBD migration does not occur from the very beginning of the drying process, but after some time; the time at which CBD migration starts and ends depends on the drying rate.

The first two aspects agree with experimental knowledge, while the third one is a modeling prediction that calls for experimental characterizations. This CGMD-based drying model can also qualitatively capture the influence of three-stage drying protocols on the electrode mesostructured. These protocols have benefits in terms of reduced manufacturing costs. In particular, it was found that applying a high drying rate at the beginning and the end of the drying and a low drying rate in the middle of the process outputs more homogeneous electrodes.

In Sim4Pro the cathode drying process is considered as the formation of the electrode structure consisting of AM and carbon-binder aggregates in DEM (LIGGGHTS). The particles are randomly generated in an RVE with periodic boundary conditions in the X and Y directions. The CB aggregates are supposed to have a high inner porosity but are depicted as non-porous particles within the simulation. Thus, the porosity is taken into account by a corresponding increase in the volume fraction. Forces for Stokes' gravity, gravity, buoyancy, compressive and capillary forces from the fluid surface, and interparticular forces are applied, assuming a constant drying rate. This results in the motion of particles to the current collector until they form a self-supporting structure, which is validated via layer thickness. However, to avoid excessive simulation times, the forces are scaled to maintain a constant ratio of settling velocity of particles and liquid surface. The model requires the drying rate, the discretized Particle Size Distribution (PSD) of the AM, the fluid viscosity of solvent and binder within the slurry, and the particle friction as input parameters. These parameters can be independently extracted from experimental measurements.

In DEFACTO the DEM is coupled to a CFD simulation (OpenFOAM) to consider fluid-particle interactions directly based on fluid simulations. Furthermore, it also allows modeling of the dissolved binder's migration in CFD. Here, the larger AM particles can be considered, on the one hand employing unresolved CFD-DEM coupling, but due to the size difference, the smaller CB particles have to be assumed as a coating on the cathode active material (CAM)particles. This approach also considers the high inner CBD porosity and leads to enlarged CAM particles. On the other hand, the resolved CFD-DEM approach is being explored to capture the fluid forces around the AM particles and the motion of CBD (considered via unresolved approach) much more precisely. The particles are randomly generated in an RVE with at least 10 CFD cells in each direction for the unresolved approach and periodic boundary conditions in the *X* and *Y* directions, of which half is filled with liquid. The liquid evaporation is depicted by a constant phase change in the CFD, surface particle interaction by a capillary force, and the dried coating is stabilized by adding a cohesion force. The binder is assumed to be dissolved so that the viscosity of the solvent-binder mixture is considered for the fluid. Additional input parameters are the mass loading, the temperature, and the drying rate. The drying rate is scaled to obtain sufficient simulation times while keeping the important force ratios constant. The simulation provides the porosity, pore size distribution, coating thickness, and the distribution of the constituents in the simulated electrode compared to experimental electrode properties for validation.

#### *3.2.3. Calendering modeling*

The simulation of the electrode calendering step is important to support the optimization between the degree of compression (aiming to improve the electronic contact between the particles) and the porosity (needed to leave space for the electrolyte to wet the electrode properly). In the case of the ARTISTIC project, DEM is used to simulate the impact of calendering pressure and speed on the electrode mesostructured by accounting explicitly for both AM particles and CBD.[46] Such a model receives as an input electrode mesostructures originated from the drying simulation (see section above). The model solves Newton Equations describing the attractive and repulsive forces between particles, namely Granular Hertzian FF describing the mechanical properties of the electrodes, and the simplified Johnson-Kendall-Roberts FF capturing adhesive forces mainly due to the binder "bridges." The FF parameters are determined by simultaneously fitting experimental microindentation and compaction curves, the former reporting the resistive force (hardness) offered by an electrode when an indentator is applied. Figure 5(a) shows the mechanical model validation of these studies by comparing the experimental (black line) and simulated (red line/dots) microindentation curve. The experimental curve corresponds to an average of 30 independent measurements, and the grey area represents the standard deviation. The experimental and simulated electrode maximal contact surface and displacement are equal to ~31000 $\mu m^2$/~18 $\mu m$ and ~11600 $\mu m^2$/~16 $\mu m$, respectively. Figure 5b shows the comparison of experimental (black) and simulated (red) evolution of the electrode porosity as a function of the applied calendering pressure. The error bars represent the experimental standard deviation. Such a model is able to capture the spatial re-organization of AM particles, CBD, and pores upon calendering (Figure 5c). Such spatial re-organization leads to a re-organization of the interfaces between the materials and pores, impacting the electrochemical performance, as can be observed by injecting the predicted electrode mesostructures in 4D-resolved electrochemical models.

Besides implementing physics-based models for the calendering steps, the application of ML approaches is essential to

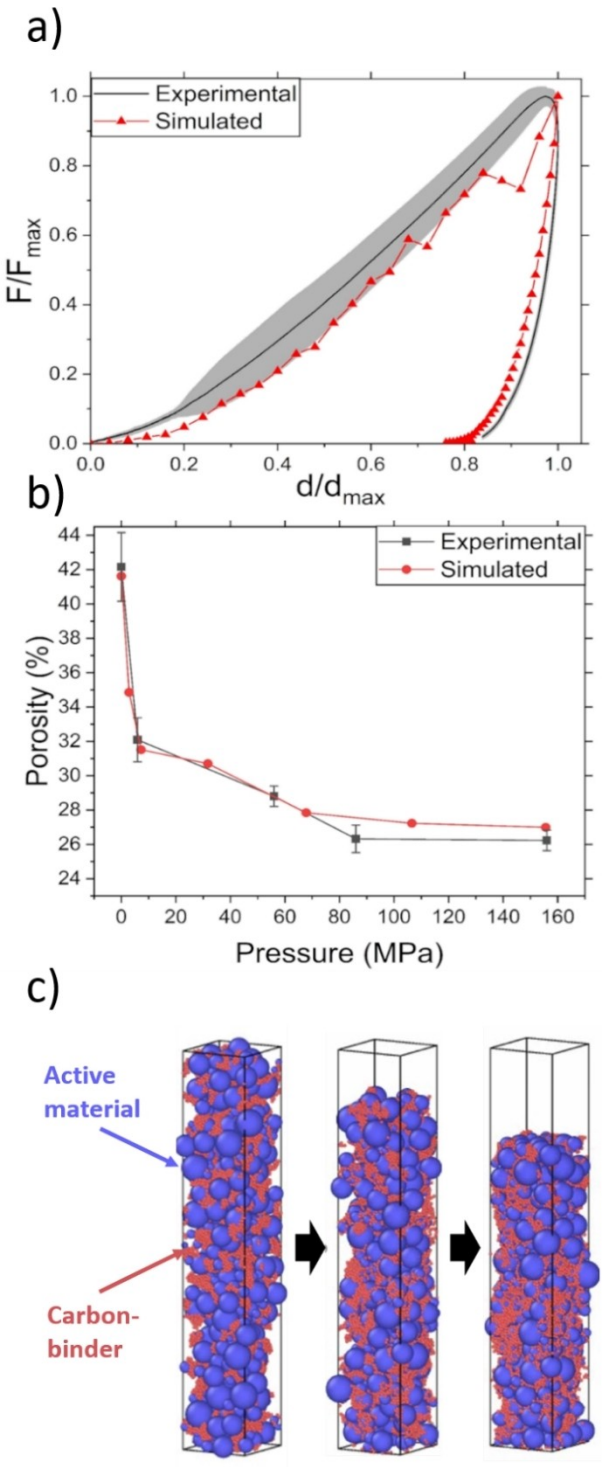


**Figure 5.** Calendering data corresponding to an NMC electrode with 96%wt AM, 2%wt carbon black, and 2%wt polymer binder. a) Experimental microindentation curve (grey) and fitted simulation results (red). b) Porosity vs. pressure experimental (gray) and fitted curve (red). c) CGMD structure evolution during the calendering process. Reproduced with permission from Ref. [46]. Copyright (2021) Elsevier.

provide deep knowledge of how fabrication parameters affect electrode properties. The latter ML fittings replace the traditional physics-based models since the calculations of corresponding properties can be eased, avoiding still more trial-error approaches and aiming to cover more combinations of parameters. However, those data can be combined with experimental measurements, paving the way to more real-world behaviors of the electrode properties to characterize better electrodes. In that sense, the calculations of electrode mesostructured properties can be assessed as a function of inputs properties, directly coming from experimental measurements. This enables to merging of synthetic and experimental datasets that are reliable enough to train a surrogate model based on well-known ML approaches. Instead of obtaining statistical conclusions which are still meaningful for qualitative purposes, the setting up of ML models reflects mathematical functions that can be tested for figuring out many other manufacturing parameter combinations. One of the ARTISTIC projects reported a study case where ML was used to predict tortuosity factors for solid and liquid phases and the percentage of contacts between different components of the electrodes. The electrode mesostructures used to train the ML pipeline were calculated stochastically according to experimental parameters such as the electrode porosity before calendering, the electrode formulation, and calendering pressure.[47]

The projects Sim4Pro and DEFACTO investigate the calendering process by numerical DEM simulations[48,49] for different material systems. As an initial structure, the CAM particles are randomly generated in a RVE with periodic boundary conditions in the *X* and *Y* directions or taken as structure from a precedent drying simulation performed by DEM (Sim4Pro) or coupled CFDEM (Defacto), which is matching the initial layer thickness, porosity, and PSD. Cylindrical bonds between the particles and the current collector allows accounting implicitly forthe CBD, which is electrically and thermally conductive. The model enables to characterize the effect of machine parameters (gap width, roll temperature, and line speed) on the heating behavior during calendering and the conductive electrode properties during and after calendering.

### *3.2.4. Electrolyte infiltration modeling*

The following step in manufacturing, electrolyte infiltration, is considered in the ARTISTIC project by using the Lattice Boltzmann Method (LBM).

This method is a relatively recent alternative to more traditional CFD simulations.[50] It considers the microscopic dynamics of fluid interactions in terms of collisions between particles and walls while obeying the constraints of the Navier-Stokes equations macroscopically. Briefly, the method divides the simulation domain into a regular lattice. A given density of the fluid is considered at each point, which evolves as virtual particles move to and from neighbors according to two movement steps. The first step considers the relaxation due to collisions between particles, while in the second step, the displacement takes place according to the velocity distribution of the particles. The LBM is highly parallelizable and provides accurate and reproducible results, particularly for irregular porous structures.[51] This allows for the in-depth study of the electrolyte infiltration process.

The lattice used by this method can be generated directly from the CGMD results from the previous step in the workflow but also stochastically generated structures or even experimentally obtained tomography images.

The main conclusions of this study[52] show how air can get trapped in isolated, very small, or poorly connected pores (Figure 6a and b). This decreases the active surface area, with negative consequences for SEI formation and, ultimately, the electrochemical performance of the assembled cell. Several variables become important to control to avoid this and other undesired effects. These include porosity, pore size distribution, and the pore connectivity network, among others, directly related to the input parameters of the previous manufacturing stages, particularly the calendering step. Additionally, the direction of the flow is identified as a critical parameter for the saturation rate and the order in which the different layers are assembled in full cells.

While the main purpose of this work was to assess the effect of different structural parameters on the rate of electrolyte saturation, the final step resulting from LBM simulations is directly exportable to different meshing programs to be later used in simulations for the assessment of their electrochemical performances. This allowed concluding that poor wettability leads to inhomogeneities in lithium intercalation and a loss of ionic conductivity.

An important limitation of this method is its high computational cost, requiring several days of calculation in a computing cluster for a typical electrode structure. This severely limits its capability to screen a large number of architectures for optimization purposes. Several options exist to address this issue. One alternative is to simply assume a total filling of the pores with electrolyte. A second one is to assume the total filling of every pore except those not connected to any other pore. Lastly, it is possible to take advantage of the large dataset that each of these simulations generates to feed data-driven models to predict saturation curves and the density of the fluid in each pore.

This latter approach has been shown to be feasible in the framework of the ARTISTIC project.[53] For this, LBM simulations can be carried out for different infiltration conditions on experimental structures. These are obtained from microtomography data corresponding to an NMC 94% – CBD 6% electrode, which yields precise information on the shape and location of the AM particles. The CBD location can be resolved using an *in-house* stochastic algorithm.[47] The resulting data, composed of the density for the electrolyte and the air phases at each lattice point as a function of time, can be processed to obtain a complete saturation curve for each pore. In turn, these data can be further reduced by selecting the saturation values corresponding to representative times throughout the simulation. The resulting reduced dataset is appropriate for training a machine-learning model based on the multi-layers perceptron approach. This yields a data-driven model capable of predicting the overall saturation curves for each pore, from which a global saturation curve can be generated. This model was validated by comparison with LBM simulations, obtaining an excellent agreement between the two for different infiltration parameters (Figure 6c).

This feasibility study allows us to draw several relevant conclusions:

- The sensitivity analysis performed for validation highlights the importance of the pore network connectivity. This calls attention to the potential usefulness of alternative manufacturing techniques such as SPS sintering or 3D printing.[54,55]
- The possibility of obtaining pore-resolved saturation values allows this method to be used as part of a workflow, yielding a final state apt to be used for subsequent electrochemical simulations for characterization.
- Once the training data is generated, this approach presents an ultralow computational cost and its low storage requirements with very high accuracy.
- While the original data corresponds to microtomography, it can be indistinctively applied to structures obtained from CGMD simulations.

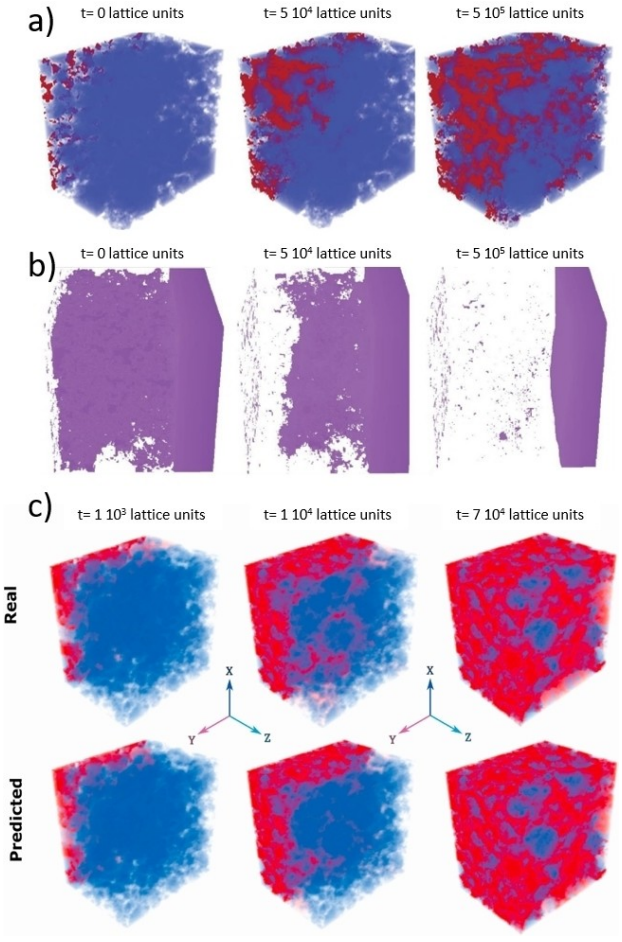


**Figure 6.** a) Visualization of the wetting process on an NMC structure obtained from tomography of an NMC 94% – CBD 6% electrode according to LBM simulations. Red represents the electrolyte, and blue the solid particles. b) Gas-phase evolution as the electrolyte displaces it. Adapted with permission from Ref. [52]. Copyright (2021) Elsevier. c) Comparison between the physics-based LBM approach and the ML-based approach. Adapted with permission from Ref. [53]. Copyright (2021) Elsevier.

Another model approach is applying CFD by using the commercially available software ANSYS. The approach detailed by Hagemeister *et al.*[56] shows two separate models for the dosing and wetting of the cell due to the different time and size scales. The mass flow is observed for the dosing simulation as the electrolyte surrounds the cell stack. The effect of pressure and temperature is studied to optimize each dosing step. The dosing will continue to gain importance as cell formats increase while the void volume in the cell decreases. Additionally, the simulations have been verified using experimental visualization from neutron radiography and show good agreement. In the wetting model, the flow through a small porous section of an NMC cathode is simulated, which can be coupled with the dosing to complete a cohesive model in further steps.

In DEFACTO, multi-scale models that integrate mesoscale and continuum approaches that optimize the electrolyte filling process are being developed. At the mesoscale, a computational approach based on LBM is used[57] to study the filling process and corresponding pore-scale phenomena in 3D lithium-ion battery (LIB) cathodes. The electrolyte flow through the nanoporous binder is simulated using a homogenization approach. Besides the processing time, the influence of structural and physicochemical properties is further investigated, guiding battery performance optimization by adapting process parameters and the electrode and electrolyte design.

### *3.2.5. Formation modeling*

The ARTISTIC project has proposed a 4D resolved model able to simulate lithiation/de-lithiation dynamics in the composite electrode mesostructures resulting from the manufacturing simulations. Such a model describes explicitly through mathematical equations the different physical processes occurring in the operating electrodes: electrochemical reaction and double-layer formation at the interface between AM and electrolyte, lithium diffusion in the AM, electronic transport in both AM and CBD, electronic transfer between the AM and CBD and lithium-ion migration (concentrated solution theory) in the electrolyte filling (totally or partially) the pores. It is worth mentioning that because of its explicit 3D nature, the model does not need input textural parameters such as particle size, active surface area, electrode porosity, or tortuosity factor, in stark contrast to classical Newman-type pseudo-2D electrochemical models. The model has been used in multiple contexts, such as the assessment of NMC111 electrodes' behavior as a function of their manufacturing parameters,[46] the mechano-electrochemical behavior of Silicon-Graphite electrodes,[32] and the simulation of impedance spectroscopy in symmetric cell conditions (beneficial for determining the electrode tortuosity factors).[58,59] The model allows assessing the impact of material distribution heterogeneities on the overall electrochemical response of the electrodes. For instance, electronic and ionic impedances are spatially resolved as they are strongly dependent on the spatial location of the different (*e.g.*, AM/CBD) interfaces.

This 4D-resolved model has also been used to simulate the SEI formation in graphite electrodes (Figure 7a).[60] By its heterogeneous nature, the model can predict heterogeneous SEI formation in the electrode mesostructured as a function of the graphite particle morphology and other textural properties (*e.g.*, porosity, tortuosity factors) related to the manufacturing process. The description of the SEI formation is performed through a simple mathematical equation relating the thickness of the SEI to the $Li^+$ concentration. The latter is calculated by solving the coupled mathematical equations describing the electrode operation, particularly the one describing $Li^+$ migration in the electrolyte. The thickness of the SEI is related to a spatially-resolved resistance which affects the local charge

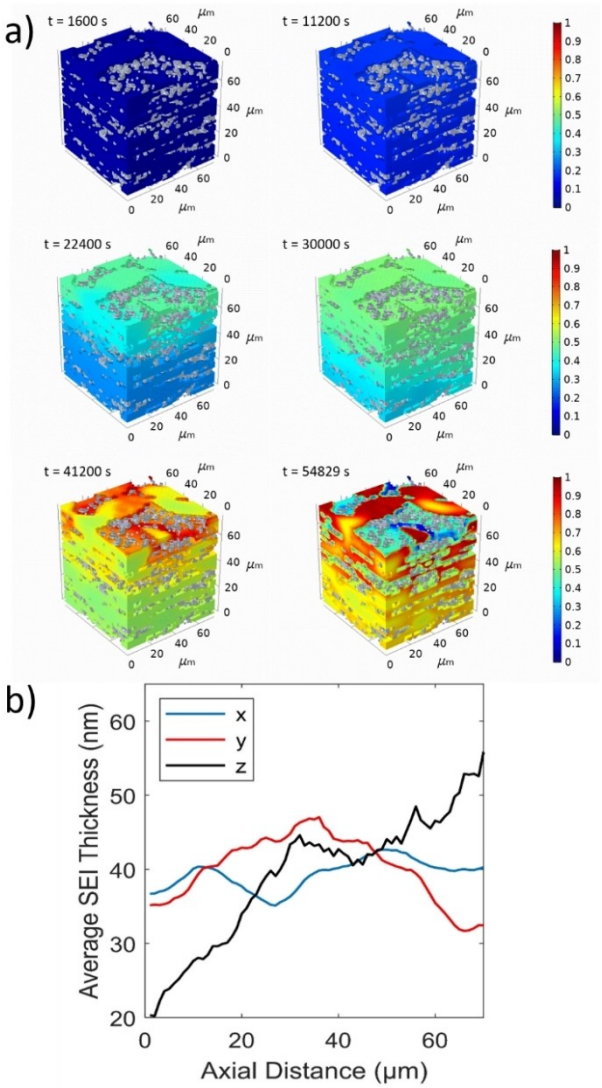


**Figure 7.** Results of the SEI formation FEM simulations for high tortuosity graphite electrodes composed of ellipsoidal AM particles. a) Snapshots of the half-cell at several stages during discharge at C/20, during which formation occurs. The color map represents the state of discharge of the AM. b) Spatial evolution of the SEI thickness in a highly tortuous electrode as a function of the cartesian coordinates, showing a heterogeneous distribution of the SEI along the direction perpendicular to the current collector. Reproduced from Ref. [60]. Copyright (2021) The Authors. Batteries & Supercaps published by Wiley-VCH GmbH.

transfer ($Li^+$ intercalation). The model was also revealed to help investigate the impact of the formed heterogeneous SEI on the performance of the graphite electrode. It was found that the thickness of the SEI becomes more homogeneous in the spherical particle electrode, where the ionic transport limitation is the mildest (Figure 7b), which leads to better electrochemical performance.

#### *3.2.6. Material and energy flow modeling of the process chain*

In addition to modeling the process-product interactions along the battery process chain (*process-oriented*), modeling the material and energy flows (*production-oriented*) in the factory is also highly relevant for battery cell production. While process-oriented modeling focuses on the quality of the intermediate and final products of the process chain, production-oriented modeling concentrates on the throughput, material, and energy demand and the degree of capacity utilization, which are key performance indicators of battery cell factories. The production-oriented simulations enable a transparent view of the material and energy flows, which allows, for example, to identify production bottlenecks,[61] energy hotspots, and the effect of energy efficiency measures[62] based on different scenarios. In particular, energy demand is highly relevant to the operating cost and the environmental impact of a battery cell factory, so that various simulation approaches can be found in the literature. The energy consumption of the production processes and the energy-intensive technical building services can be modeled by mechanistic[63] or data-based[64] approaches.

In production-oriented simulations, different modeling paradigms, such as *agent-based*, *discrete event*, and *dynamic systems*, are coupled to describe the material and energy flows along the process chain.[65] Agent-based modeling describes active objects such as production machines or product units. Discrete event modeling characterizes the internal behavior of the agents by different states which are connected via specified conditions. Dynamic systems modeling is used to characterize the temporal behavior of, for example, the electric power demand or the material flow. Integrating the different simulation modeling paradigms in software such as Analogic or Plant Simulation allows a dynamic description of the material and energy flow in battery cell factories.

Similarly, Schönemann *et al.* proposed a multi-scale simulation approach that combines multiple factory levels in a modular platform.[66] The core element is the process chain module, which defines other factory elements, such as the production machines, processes, product flow, workers, or technical building services. Individual model approaches can characterize each factory element. The heterogeneous models are synchronized efficiently via middleware and thus enable an elaborate description of the energy demand of a battery cell factory.

In addition to the process equipment, the technical building services (TBS) contribute significantly to the energy demand in battery cell production. The recovery of the organic solvent (NMP) during drying is essential due to the toxicity and the inherent value of the solvent. Ahmed *et al.* introduced a spreadsheet model based on mass and energy balances for the drying process with a subsequent solvent recovery, where the power demand, temperatures, and NMP contents are described for the individual elements of the drying and recovery equipment, i.e., electrode dryer, condenser, chiller, zeolite wheel.[67] The authors showed that solvent recovery imposes 45 times higher heat demand than needed to vaporize the NMP.

Furthermore, the energy demand contributed by the dry room immensely affects the overall energy demand required for battery cell production (up to 48% of overall electricity demand).[68] It thus has been the focus of recent modeling works. Physical simulation models provide a dynamic assessment of the energy demand as a function, e.g., the weather condition or workers inside the dry room. Modeling languages such as Modelica are used to describe the humidity, airflow, and temperature within the different components of the technical building services, such as the process fan, regeneration fan/heater, pre-cooler, or supply air heater.[69] The model results provide essential knowledge for the planning and operation of dry rooms for battery cell production.

#### *3.2.7. Assembly modeling*

In addition to image-based defect detection techniques, traditional Failure Mode and Effects Analysis (FMEA) and simulation techniques are also used to design and optimize assembly and manufacturing processes. The finite element method (FEM) is widely used in the design phase of the cell assembly process. Schilling *et al.* simulated the stresses generated during the winding process. The mechanic characterization approach adopted can determine the minimum bending radius for manufacturing electrode-separator-composites.[70] The HoLib project team[71] from the Prozell cluster also reported using dynamic finite element analysis (FEA) to simulate the cutting process of electrode sheets. In one of the articles of this team[72] the FMEA method is applied to the electrode stacking process. Based on a failure mode ranking, the positioning error of the electrode foils is considered in detail, and an algorithm to simulate the stacking error is presented in Matlab.

### 3.3. Models implementation in practice

In terms of physics-based models, the manufacturing process of LIBs has been mainly considered using CGMD and DEM simulation techniques. Later steps include electrolyte infiltration, which requires fluid dynamics simulations and electrochemical simulations that FEM can implement. Table 3 presents some examples of software that can be used for these purposes.

LAMMPS is an open-source classical MD code developed by researchers from the US Department of Energy in collaboration with other private centers and universities. The code, written in C++, is also parallelized with MPI, allowing for very efficient and fast simulations. LAMMPS's objective materials are solid-

**Table 3.** Software typically used for the mechanical modeling of the manufacturing process.

| Software | Type | Reported applications |
|---|---|---|
| LAMMPS | Open source | Slurry,[30] drying,[45] calendering[46] |
| LIGGGHTS | Open source | Calendering[46] |
| Palabos | Open source | Electrolyte infiltration[52,53,73] |
| Abaqus FEA | Commercial | Coating and calendering,[74] winding,[75] welding[76] |
| COMSOL Multiphysics | Commercial | Formation[32] |

state systems such as metals or semiconductors and soft matter systems like biomolecules and polymers, as long as the modeled interactions are short-ranged and particle densities are moderately bounded. LAMMPS has available the so-called ML potentials, which replace the physics equations fit a set of experimental or calculated data with generic equations that describe the geometry of a neighborhood of atoms and are refined with an increasingly large dataset.[77]

LIGGGHTS is another open-source software developed by CFDEM® project based on LAMMPS, but with a special focus on DEM for industrial applications. For this purpose, it expands on the latter basic capabilities to include the possibility of importing complex geometries, moving meshes, improvements on the code dealing with granular interactions, description of heat conduction, and the possibility of coupling with CFD simulations, among others.[78]

Palabos is a C++ library for CFD simulations based on the LBM. It can be accessed through Python or Java interfaces, facilitating its use and easily setting up simulations without the need for a deep understanding of the LBM algorithms. Additionally, it works on various platforms due to its general lack of dependencies. Palabos takes advantage of the highly parallelizable nature of LBM to allow for the use of MPI libraries that work efficiently, leading to a significant improvement in calculation times.[79]

COMSOL Multiphysics and Abaqus allow running FEM and DEM simulations for mechanical, electrical, and electrochemical applications. Simcenter STAR-CCM+ is a multiphysics CFD software that focuses on optimization. Simcenter Battery Design Studio allows the simulation of LIB cell performance with a wide array of battery components and materials.

Due to the improved interconnectivity of devices, the overall increase in computational power and a higher degree of data availability enable applications of data-driven methods. These methods are capable of extracting (or mining for) desired information from vast amounts of data. Many of these methods, such as ML or AI, are commonly applied in everyday situations (e.g., self-driving cars and recommendation systems in online shopping). Although these algorithms and methods are highly sophisticated and complex, their application hurdle has been greatly reduced over recent years. This has been achieved by developing various data analytics tools (e.g., RapidMiner, KNIME, ELKI). The former requirement of being capable of creating your code or algorithms is no longer given using these tools. Many data analytics tools offer built-in functions that only have to be parameterized before analyzing the data. However, programming and scripting languages (e.g., Python, R, Matlab) are still widespread in the scientific world. They have many highly specialized libraries to support the customizability and application of state-of-the-art algorithms. In the following, the most common data analytics tools and programming/scripting languages are presented and explained in detail in Table 4, with corresponding studies applying those in battery production.

## 4. Data Specifications

### 4.1. Manufacturing parameters

In order to encode computational models in digital twins capable of performing on the fly optimization of the manufacturing process, it is important to have a clear overview of the type of data is involved in the process of flowing information from the real prototyping line to the digital twin and from the latter to the former (cf. Figure 1). In the following, we present a classification of LIB manufacturing data types regarding their future use in digital twins of prototyping lines. This classification intends to provide a template that quickly identifies the missing gaps and defines practical recipes for digital twins development and implementation.

The manufacturing parameters strongly impact the electrode meso/microstructure and the cell properties. The output properties of each manufacturing step affect the output properties of the subsequent steps with a degree of impact, which depends on the specific parameters under consideration (e.g., materials chemistries or AM PSD).

The following subsections correspond to each step of the manufacturing process. A description is given for the parameters relevant to each step, how they are measured, and the accuracy that state-of-the-art sensor technology can provide. Next, the importance of these parameters as inputs in models is briefly presented. To this end, models have been classified into four categories: empirical models are simple relations that can be found by simply fitting experimental data to mathematical functions; continuum models are physics-based models that generally rely on a set of Partial or Ordinary Differential Equations that describe the underlying behavior of well-known physical phenomena; discrete models usually consider the system as composed of individual particles following simple rules that determine the complex emerging behavior of the whole system; finally ML models are not based on any physical insight but rather try to predict a system's behavior from the aggregation of similar previously available data.

All the input parameters below are considered important in determining the output parameters for each manufacturing step. This criticality refers to the importance of knowing a parameter for setting and validating each type of modeling approach aiming to predict the influence of manufacturing parameters on the output of each step. Models (particularly true for ML ones) can be designed in principle to deal with all the parameters, but here we refer to what the models reported in state-of-the-art can currently account. Each section ends

**Table 4.** Data-driven modeling software tools and programming languages.

| Tool | Description | Studies | Program languages | Description | Studies |
|---|---|---|---|---|---|
| RapidMiner (former YALE) | Java-based science and ML platform<br>Node-based workflow<br>data loading, transformation, and preprocessing, visualization, analytics and modeling, evaluation, and deployment | Schnell *et al.*[80] | Python | Interpreted high programming language<br>Eased readability and a low entry barrier<br>Many specialized libraries for mathematics, science, ML, etc. | Severson *et al.*[81]<br>Thiede *et al.*[64]<br>Liu *et al.*[82]<br>Turetskyy *et al.*[83]<br>Vogt *et al.*[84]<br>Niri *et al.*[85] |
| KNIME (Konstanz Information Miner) | Java-based free and open-source data analytics and reporting platform<br>Node-based workflow<br>data loading, transformation, and preprocessing, visualization, analytics and modeling, evaluation, and deployment | Bockwinkel *et al.*[86] | R | Interpreted programming language<br>Many specialized libraries for statistics, mathematics, science, etc.<br>Can implement code from C & C++ | Kornas *et al.*[87]<br>Cunha *et al.*[33]<br>Kirchhof *et al.*[88]<br>Meyer *et al.*[89] |
| Others | ELKI (Environment for developing KDD-Applications Supported by Index-Structures)<br>Weka (Waikato Environment for Knowledge Analysis)<br>SPSS<br>H2O.ai | Kornas, *et al.*[90] | Matlab | Proprietary programming language<br>Allows faster and computationally more efficient matrix operations compared to other programming languages<br>Many specialized libraries for statistics, broad engineering fields, computer vision, ML, etc. | Westermeier *et al.*[91]<br>Severson *et al.*[81]<br>Duquesnoy *et al.*[47]<br>Liu *et al.*[92]<br>Rynne *et al.*[6]<br>Chen *et al.*[93] |
| Azure Machine Learning (Microsoft) | Cloud-based environment for developing ML projects at big scales<br>Data management, predictive modeling, deployment | | C (C#/C++) | Compiled high programming language<br>Higher entry level<br>Very fast execution due to efficient mapping to machine instructions<br>Widely used for embedded applications | Lombardo *et al.*[30] |

with a table that will allow the readers to quickly and graphically visualize the criticality of these parameters through a color scale with three levels: red for high, yellow for intermediate, and blue for low. These tables also present columns related to measurability that show how easy it is to acquire these data in the pilot plant and the available accuracy. For the measurability columns, blue indicates great difficulty, yellow indicates intermediate difficulty, and red is easily measurable. For accuracy, blue means poorly accurate, yellow means moderately accurate, and red means highly accurate. The color-coding has been assigned based on the technique's straightforwardness to measure and accuracy for characterizing the referred parameters. We discuss essentially the parameters in each manufacturing step section that are poorly accurate and greatly difficult to measure. Of course, the color-coding could be influenced by the pilot line development and experience; we consider it a helpful aid as initial and easy-to-read. It is important to note that these rankings arise from an interative discussion along monthly meetings for an entire year between the different pilot line groups involved in the Expert Group "Digitalization, Measurement Methods and Quality" of the EU Li Planet Network. The last column indicates whether the measurement can be made in real-time during production (online) or needs to be made separately (offline). The tables also divide the parameters into three categories: machine parameters (MP), which are externally controlled inputs (e.g., formulation, solid content, mixing speed), process parameters (PP), which cannot be controlled externally but are the result of the chosen MP, and they have an effect on the result of each step (e.g., slurry viscosity, density forces generated by the mixing) and structure parameters (SP), which are resulting or output properties (e.g., porosity, tortuosity factor, effective electronic conductivity). Some of these MP and PP parameters influence the SP more than others, and the interdependencies are expected to be highly nonlinear.[94] Reporting such non-linear dependences is a challenging process, and while this is out of the scope of this article, we intend to address this in a future publication.

#### *4.1.1. Slurry*

The materials selected for electrode preparation are based on the required cell characteristics. Multiple techniques need to be used for complete characterization, which is relatively easy to measure and highly accurate. For instance, the chemical composition and the impurities or the surface components generated by the materials can be measured by a combined analysis with microscopy, XRD, XPS, or Raman spectroscopy. For impurity and elemental analysis, inductively coupled plasma (ICP) can also be used for detecting pollution in the parts per million range. However, when using this technique, sample and calibration standard preparation are a major concern because of the risk of contamination from sample containers and chemical reagents.[95] The morphology of the active materials and the conductive additives is characterized by microscopy. Different techniques can measure the particle size distribution (PSD) depending on the measuring principle (i.e., laser diffraction, dynamic light scattering, imaging) since particle size distribution is a significant parameter for electrode slurry preparation. A difficulty when measuring PSD and morphology arise when the particles agglomerate or their shape is not homogeneous, impacting the measurability and accuracy of the result.

Once the raw materials are characterized, the slurry recipe is defined, including the active materials, the conductive additive, and the binder content. Also, the solid content that determines the solvent amount needs to be decided. Those input parameters are usually measured using a weighing balance.

Generally, the slurry is a system of suspended particles that is not in equilibrium. It is mainly composed of solvents, active material particles of micro- or sub-micrometer size, conductive agents, and binders of sub-micrometer size or even smaller than 100 nm. The particles tend to sediment and aggregate depending on their size, density, and shape, during and after slurry manufacturing. The electrode manufacturing process is a long and continuous process in which coating is not always possible immediately after slurry preparation, so the slurry must remain stable during the storage period before coating. For this reason, the dispersion of the components is a crucial factor affecting the rheological behavior of the slurry. Poor slurry stability and homogeneity can lead to settling of the components and weakening the overall performance and production efficiency of the coated electrode, which is detrimental to the quality of the battery.

The stability, homogeneity, and processability of a slurry are characterized by rheology. Liu *et al.*[14] have introduced basic rheology concepts in the context of LIB electrodes. The most influential rheological feature of a slurry is its viscosity, which is impacted by several properties such as particle size, shape, roughness, charge, thermodynamic and hydrodynamic forces, and solid fraction.[13,16]

Different mixers such as ball milling, planetary mixers,[96,97] high-speed mixers, homogenizers, universal type mixers, and static mixers have been developed to be generally used for slurry mixing step. Ball mixer is industrially accepted as a reference tool despite its high energy consumption and limited practicality for large-scale production.[16] At the same time, the shear mixer (i.e., the planetary mixer) is the preferred choice for industrial applications.[13] The most important parameters to consider during slurry processing are rotational speed and time. These parameters vary depending on whether a slurry is prepared for the cathode or the anode. They can directly influence the resulting viscosity, depending on their ability to disperse the particles and prevent the formation of agglomerates caused by the interaction of the materials. These values are found between 1000–4000 rpm and 10–120 min for both cases. Another parameter that affects slurry properties is temperature, especially for slurries containing NMP. Generally, slurries are mixtures with non-Newtonian behavior easily affected by temperature changes.[98] Hawley and Li[99] evaluated the behavior of cathode slurry mixing in a temperature range between 25 and 75 °C. They demonstrated that at 60 °C better slurries are obtained with properties more suitable for faster and longer coatings. Despite the significant influence that temperature can have on the properties of the resulting slurry, relatively not much literature is available on this subject.

As mentioned above, the most influential characteristic of rheological properties is viscosity, which is characterized offline by rheology measurements at a shear rate relevant to the coating process. Standard rheometers cover very little of the range of shear rates encountered in coating (typically $10^{-1}$–$10^{3}$ $s^{-1}$). Frequently, a shear rate is picked depending on the lower limit of the coater. If the viscosity is low enough at this point of interest, it will flow in the coater since these instruments have some constraints. For instance, a thick slurry is difficult to be applied homogenously through the current collector, while a thin slurry could produce thickness variations and spillage.[13] If a sweep of shear rate is performed, extrapolations of the viscosity to higher shear rates can be performed, e.g., assuming that the material follows power-law behavior.[100]

Other techniques that have recently attracted attention to measure the aggregates and the slurry homogeneity are the Zeta Potential and inverted microscopy due to the facility to measure the particle size of samples suspended in liquids in the size distribution range of 0.1 nm to 12 μm at different concentrations. The information obtained is directly related to aggregates and the slurry homogeneity.[101–103] Nevertheless, for these techniques, it is necessary to dilute the slurry. As it is well known, solid content variations may directly impact the particle aggregation and slurry homogeneity, resulting in challenging and indirect to measure (assigned blue in Table 5).

Continuum models used to describe the mixing process can use the solid content and mixing parameters as inputs to predict the rheological properties of the slurry.[104]

Published discrete models for slurry preparation are mostly based on CGMD. These models explicitly consider formulation, solid content, and particle size distribution; they implicitly consider other process parameters such as carbon additive size, purity, and materials chemistries through the FF parameters, which need to be fitted to experimental data. The mixer type, rotational speed, mixing time, and ambient conditions are usually disregarded, assuming thorough mixing. A full simulation of this process would require considering full-scale systems (out of reach of current computational capabilities) or the use of simplified model systems that allow only for the qualitative study of general trends. In terms of structure parameters, density, viscosity, homogeneity, aggregate size, and other rheological parameters are useful quantifiers to fit the model. They are the main outputs of the discrete models. In particular, density and viscosity are used to fit the model to experimental results.

ML models are already well known for treating the explicit material, formulation, and solid content as input variables to analyze their effect on the coated electrode and even on the final electrode properties. Moreover, it appears possible to consider electrode properties from the slurry as inputs (e.g., viscosity) instead of fabrication parameters.[30] This is especially true when optimizing the slurry manufacturing modeling, dealing with FF parameters of the corresponding physics-based models. The fitting of electrode properties, like the viscosity or mass loading, enables bypassing the experimental measurements to predict these properties as a function of various manufacturing conditions. This considerably reduces the trial-and-error approaches done in experiments.[33] In the end, the various batch of electrode properties coming from the

**Table 5.** Summary of the parameters relevant to the slurry preparation step.

| Slurry preparation | | Importance[d] (criticality) Empirical | Continuum | Discrete | ML | Measurability[e] | Accuracy[f] | Online/ Offline[g] |
|---|---|---|---|---|---|---|---|---|
| MP[a] | Material storage conditions | N/A | | | | XPS, Raman Spectroscopy | Few nm – few µm | Offline |
| | Materials chemistries | | | | | XPS, Raman Spectroscopy | Few nm – few µm | Offline |
| | Formulation (ratio) | | | | | Balance | Percentage | Offline |
| | Solid content | | | | | Balance | Percentage | Offline |
| PP[b] | Active material PSD | | | | | Microscopy XRD | Å to µm | Offline |
| | Active material particle morphology | | | | | Microscopy | Few nm – µm | Offline |
| | Carbon additive size | | | | | Microscopy | Few nm | Offline |
| | Purity | | | | | Magnetic separator, Microscopy, ICP | | Offline |
| MP | Mixer type | | | | | Set-up design | | – |
| | Mixer rotational speed | | | | | Control parameter (MP) | rpm | Online |
| | Mixing temperature and ambient conditions | | | | | Control parameter, thermostat | ±1 °C, Humidity < 1.0 % | Online |
| | Mixing time and sequence | | | | | Control parameter | min | Online |
| SP[c] | Aggregates size | | | | | X-ray CT method, Inverted Microscopy, Zeta Potential Determination by Electrophoretic Light Scattering, Laser diffraction spectrometer | 0.1 nm to 12 µm | Offline |
| | Homogeneity | | | | | | Days/0.1 nm to 12 µm | Online |
| | Microstructure | | | | | | | Offline |
| | Density | | | | | Densimeter | g $cm^{-3}$ | Offline |
| | Viscosity *vs.* shear-rate | | | | | Rheometer | Pa s *vs.* $s^{-1}$ | Offline |
| | Other rheological parameters | | | | | Rheometer | Pa vs. Hz | Offline |

[a] Machine parameters (MP), which are externally controlled inputs. [b] Process parameters (PP), which cannot be controlled externally but are the result of the chosen MP, and they affect each step's result. [c] Structure parameters (SP) are resulting or output properties. [d] Criticality for setting and validating the modeling parameters evaluated as: red for high, yellow for intermediate, and blue for low. [e] For the measurability columns, blue: great difficulty, yellow: intermediate difficulty, and red: easily measurable. [f] For accuracy, blue is poorly accurate, yellow is moderately accurate, and red is highly accurate. [g] The measurement can be made in real-time during production (online) or needs to be made separately (offline).

experimental measurements and the outputs of physics-based models serve as meaningful variables for the ML models while optimizing the slurry step, which is the most critical step of the full fabrication process.

Table 5 summarizes the above information in an easy-to-read, color-coded way.

### *4.1.2. Coating*

In the coating step, the suspension is applied to a current collector with an application tool, either continuously or intermittently. The coating is applied while the current collector is supported by a roller or tensioned by a set of rolls.[100]

The coating set-up significantly impacts the properties of the manufactured electrodes with a typical coating speed (0.3–30 m/min). Slot-die coating is currently the most common industrial practice due to its closed system being less prompt to environmental conditions. In contrast, doctor Blade is the most used procedure on the laboratory scale. A pump supplies the slurry during slot-die coating, and the flow rate and slot width determine the volume of the slurry. In comparison, the doctor blade or comma bar coating is self-calibrated, and the gap set determines the slurry volume allowed. Advantages of this slot die method compared to the lab-scale coatings are, e.g., the precise dosing, easily scalable process parameters, and closed feed system.[105,106] There are also novel coating techniques under development, spray coating,[107] electrophoretic deposition,[108] and 3D printing,[109] among others; however, in the context of this paper, we are focusing on the most applied technique, such as the slot die.

The most influencing machine parameters in the slot die coaters are the coating speed, web tension, and coating gap, whose accuracy depends on the machine gauge precision (accuracy assigned as yellow in Table 6). The challenge remains to identify the base operating windows that favor and are directly related to homogeneous electrode structure output parameters. Generally, the structure coating output parameters such as surface homogeneity, wet-fil thickness, adhesion, and defects are mostly intermediate to measure with resulting average accuracy (assigned yellow in Table 6) and will be discussed hereafter. Coating defects can occur outside the proper coating ranges, such as ribbing, dripping, rivulets, and air entrainment.[34] Coating speed directly impacts the formation of edges on the electrode film, particularly during intermittent coating. Therefore, it is necessary to control the coating speed and fluid supply since the wet-film thicknesses differ depending on it, especially at the edges.

Another critical parameter is the coating gap, which is directly related to the final mass loading of the electrode and hence the theoretical cell energy density, one of the most important outcomes for a defined manufactured cell. Depend-

**Table 6.** Summary of the parameters relevant to the coating step.

| Coating | | Importance (criticality)[d] Empirical | Continuum | Discrete | Measurability[e] | Accuracy[f] | Online/ Offline[g] |
|---|---|---|---|---|---|---|---|
| MP[a] | Coating set-up | | N/A | | Set up design | – | Online |
| | Speed | | | | Control machine | ±0.05 m/min | Online |
| | Gap | | | | Control machine | ±1 μm | Online |
| | Web tension | | | | Control machine | ±0.05 N | Online |
| | Ambient Temperature | | | | Thermocouple | ±0.5 °C | Online |
| PP[b] | Slurry rheological properties | | | | Rheometer | Pa s vs. $s^{-1}$<br>Pa vs. Hz | Offline |
| | Slurry particle size | | | | Inverted microscopy, X-ray CT, Zeta Potential Determination | 20 nm to 12 μm | Offline |
| | Surface homogeneity | | | | Camera, light sensor | – | Online |
| SP[c] | Wet film thickness | | | | Laser triangulation | ±0.5 μm | Online |
| | Defects | | | | Camera | ±0.5 μm<br>–<br>– | Online<br>Online<br>Online |
| | Edge geometry | | | | Camera | – | Online |
| | Adhesion | | | | Trigger test, Peel Test 90° Uniaxial-material testing machine | ±0.05 N/m | Offline |
| | Loading | | | | Beta gauge, Ultrasound | ±0.01 mg/$cm^2$ | Offline |

[a] Machine parameters (MP), which are externally controlled inputs. [b] Process parameters (PP), which cannot be controlled externally, but are the result of the chosen MP, and they have an effect on the result of each step. [c] Structure parameters (SP), which are resulting or output properties. [d] Criticality for setting and validating the modeling parameters evaluated as: red for high, yellow for intermediate, and blue for low. [e] For the measurability columns, blue: great difficulty, yellow: intermediate difficulty, and red: easily measurable. [f] For accuracy, blue: poorly accurate, yellow: moderately accurate, and red: highly accurate. [g] The measurement can be made in real-time during production (online) or needs to be made separately (offline).

ing on the application, the desired electrode could be thick or thin based on the coating gap. For thicker electrodes, the energy density increases, but it also complicates the transport limitation provoking certain electrode polarization. Therefore, a compromise between the optimum thickness and electrode properties is necessary, like the porosity, tortuosity factor, and homogeneous material distribution. From a technical standpoint, a thick electrode (>500 μm) can be challenging to manufacture because of its slurry weight, density and rheological properties.[110] The last two related to ambient temperature and will affect the uniformity of the coating. This parameter is directly linked to the fluid rheological properties. For instance, viscous slurries cause problems in the coating process, resulting in low film uniformity.

On the other hand, a low viscous slurry will trickle when using a thick comma gap. Consequently, the slurry viscosity must be adapted when using a too large coating gap.[110] Thin electrodes are particularly interesting for high-power applications. When producing a thin electrode, the coating gap needs to be reduced. The minimum achievable gap depends on the agglomeration or particle size that is normally characterized when preparing the slurry (measurability and accuracy discussed in Section 4.1.1). Likewise, agglomeration and slurry particle size may provoke surface electrode inhomogeneity because big particles (bigger than the coating gap) tend to leave traces on the coated electrode. When using slurry quantities (<50 L), it could be advantageous to filter the slurry, however important material losses are expected.

Another important parameter to consider during coating is coat-weight uniformity. Lower mass loading electrodes will have more impact if there is a higher variability than high-energy electrodes. The coat-weight uniformity highly depends on the slurry rheology, like the coating thickness factor. Variations in the current collector thickness, coating speed, and slot-die design will highly impact the coating homogeneity, hindering its accuracy and measurability.[110]

The micrometer and balance are the most commonly used tools for measuring coating thickness and mass at the lab scale after drying. These methods are offline and cannot represent the variations through the entire electrode roll. Laser triangulation and calipers are usually employed for online measurements because they are accessible, nondestructive, and capable of estimating and identifying the coating process and defects.[100] Coating defects such as film instability and edge effects can generally occur. They must be controlled within the online operation to avoid huge scraps or manufacturing cells that can lead to premature degradation. The wet-film thicknesses can be measured by using a 2D triangulation system. It has been observed that the volume flow decreases for the different coating speeds, provoking a decrease in the wet film thickness, thus the formation of edges.[111]

Certain empirical approximations can be found in literature where the correlation between the coating parameters and

their impact on the film uniformity is analyzed. Ding *et al.*[34] reviewed different coating limits such as various vacuum pressures, low-flow, dynamic wetting failures, wet thickness for zero-vacuum-pressure cases, and coating speed for a specific flow rate.

Continuum scale studies on CFD models have gained more attention in the last few years. These models can reveal and provide an understanding of the characteristics of the flow field near the dynamic contact line, which is key to understanding the mechanisms of coating defects. In this regard, 2D Navier-Stokes equations have been used to describe the behavior of the flow field in the coating bead.[37,38,112,113] However, there are still no complete physical equations describing the impact of the coating parameters.

ML can be used to assess the impact of parameters such as the gap of the coating step, together with slurry formulation and solid-to-liquid ratio, on the electrodes' heterogeneity.[39] Other approaches include different formulations, manufacturing protocols, and performance properties. For instance, input parameters from formulation and manufacturing were varied like slurry composition, mixing protocol, electrode coating gap size, drying temperature, coating speed, and calendering.[40]

Table 6 summarizes each parameter's criticality in the corresponding modeling approach and the most important parameters involved in the coating.

#### *4.1.3. Drying*

Directly after the coating step and before the drying process starts, the wet film supported onto the film has almost homogeneous particle and additive distribution within the solvent. In this step, the coating is fixed on the current collector surface, consolidating the uniform electrode structure and morphology formation to achieve the desired cell performance. This is completed by evaporating the solvent from the slurry with a typical drying rate of 25–50 m $min^{-1}$.[114]

Hot-air convection and infrared radiation drying are among the most common drying techniques,[115] although we focus on the hot-air drying type in this work. Under hot air, in the first stage of the drying process (film shrinkage), the solvent evaporates from the film's top surface, causing it to shrink until the rigid AM particles make contact with each other, stopping any further decrease in film thickness. Then, the second stage of drying (pore emptying) is initiated, in which the solvent in the pores between the AM particles evaporates.[99] At this stage, the solvent molecules diffuse through the thickness of the electrode shifting the AM particles, the binder, and conductive additive (binder/conductive additive migration), leading to reduced contact between the current collector and the electrode.[18,116,117] It is thus necessary to find the best compromise between minimizing the binder migration and the drying rate protocol to avoid weak electrode/current collector adhesion that may produce capacity fading and mechanical failure (*e.g.*, electrode delamination from the current collector.

In general, there are five main parameters to be considered when operating the dryer: the drying type, speed of the rolls, the drying temperature or drying rate, the hot air flow (*i.e.*, air velocity), and energy consumption.[118] Similarly, as we discussed in the previous section, machine parameters impact morphological and structural output electrode characteristics. For instance, the roll speed parameter directly impacts the electrode's homogeneity and quality, provoking defects such as pins, holes, cracks, and delamination. Another critical parameter is the drying rate. In this case, it has been observed that higher drying rates and temperatures lead to higher binder migration and poor adhesion strength. An unsuited drying protocol provokes defects in the electrode, such as mud-cracking and curling. There is the stress generated when using drying faster protocol rates, where the top surface of the electrode dries faster than the rest of the coating. The solvent molecules trapped at the bottom of the electrode become active, causing the top layer to fracture. Thus, line speed is related too with protocol rates when producing electrodes depending on the thickness. Therefore, these parameters should be optimized and are influenced by the electrode coating composition, thickness, and mass loading. Consequently, understanding the individual or combined effects of these parameters on the dried electrodes is essential for optimizing and improving the resulting electrode structure.

This resulting electrode micro/mesostructure, including the binder distribution of the electrode after drying, is characterized by ex-situ AFM, SEM, TEM, and EDX, among others. These techniques have demonstrated the ability to distinguish between the binder distribution, conductive additive, and AM. However, poor accuracy and measurability can arise from differentiating materials with similar chemical or morphological environments.[119,120] The peel test measured the electrode adhesion strength offline, separating the coating from the current collector using tapes.[121] This test provides comparative information between electrodes produced in-house. Because it employs different variables such as tape type, placement, tape application, and measurement machine, which can change from other pilot planes, hindering the measurability and accuracy from comparing with outsider reported adhesion properties.[122] Different online methods are currently available to monitor the electrode drying step. The laser scanning confocal microscope technique is already known to evaluate the roughness of the electrode in place.

Moreover, laser triangulation or even the online laser caliper is also used to monitor the thickness of the dried electrodes. In addition, through IR cameras, the temperature profile of dried electrodes can be monitored. These mentioned techniques can expose any potential electrode coating defects.

Design of Experiment (DoE) is a widespread methodology in the industry as part of FMEA to identify and classify influencing parameters. In reference,[123] DoE methodology is employed for the pilot-scale manufacturing of NMC622 cathodes to determine the main influencing process variables of the coating-drying step. In this work, empirical models representing the relationship between the operating variables (i.e., temperature, speed), electrode and cell physical characteristics, and the cell electrochemical performance were obtained by linear regression.

Continuum scale modeling can help validate hypotheses and better understand the key parameters influencing electrode structure formation in the drying step. In this regard, the 1D model is the most common approach.[18,124,125] However, in most cases, this is valid only for a specific part of the whole drying process, either the initial film shrinkage stage or the subsequent pore emptying stage). Neither of these existing models can be relied upon to predict the whole optimal LIB electrode drying step.[114]

CGMD models consider the solvent only implicitly, and thus, its evaporation deals by using a change of FF parameters. The machine parameters are weighted using a few parameters related to the conversion rate from the "wet" state to the "dry" form and the difference in conversion rate between horizontal layers of the domain. This approach describes some critical phenomena during drying and identifies trends, but it is challenging to translate to experimental parameters quantitatively. As structure parameters, porosity, microstructure, and binder distribution are all well described by this approach. In contrast, some larger-scale features like surface roughness, defects, homogeneity, and cracks can be accounted for but require the set up of very large simulation domains, which could be beyond the reach of currently available computing resources. CFD-DEM coupling method is also used to understand particle-particle and particle-fluid interactions within the drying step. Through this approach, electrode shrinkage along this step can be properly understood.

ML models usually consider the coating speed, temperature, gap, and the speed and temperatures from the drying step as critical fabrication parameters to evaluate better fabrication conditions.[126] Indeed, they are the most significant electrode properties (e.g., thickness, mass loading), representing the common ML outputs. More precisely, the assessment of many measurements per condition can be analyzed with these ML models by directly predicting the average value and standard deviation corresponding to one fabrication process. The same electrode properties define new electrode performance criteria (*e.g.*, heterogeneity) to optimize manufacturing and the best fabrication processes. Table 7 summarizes the above information in an easy-to-read, color-coded way and the criticality of the corresponding modeling approach and the experimental parameters.

### *4.1.4. Calendering*

Calendering is the last electrode fabrication process step. Here, the electrodes are compressed between two rollers. During calendering, the final electrode thickness and porosity are defined. Moreover, the particle-to-particle cohesion and cast electrode-to-current collector adhesion, mechanical properties of the electrodes, and electronic conductivity are improved when compacting the electrodes.

The most relevant machine input parameters are the gap between the two calendering rollers, the pressure applied to the electrodes, the calendering speed, and temperature. Depending on the desired electrode/cell characteristics (high energy/high power cells), the values for these parameters are selected. Electrode characteristics also influence the calendered electrode properties. Usually, cathode electrode AMs are harder than graphite; therefore, the former is more difficult to compact. On the other hand, the density of active cathode

**Table 7.** Summary of the parameters relevant to the drying step.

| Drying | | Importance (criticality)[c] Empirical | Continuum | Discrete | ML | Measurability[d] | Accuracy[e] | Online/ Offline[f] |
|---|---|---|---|---|---|---|---|---|
| MP[a] | Drying type | | | | | Set up design | N/A | |
| | Line speed | | | | | Control (MP) | ±0.05 m/min m /min | Online |
| | Airflow | | | | | Control (MP) | ±0.5 $m^3$/h $m^3$/h | Online |
| | Temperature/ drying rate | | | | | Control (MP) | ±0.5 °C | Online |
| | Energy consumption | | | | | N/A | W h | Online |
| | IR-Radiation | | | | | Control (MP) | | Online |
| SP[b] | Surface roughness | | | | | Laser scanning confocal microscope | µm | Online |
| | Defects | | | | | IR thermography | °C | Online |
| | Homogeneity in thickness | | | | | IR thermography | µm | Online |
| | Fractures and mechanical properties | | | | | Camera, Microscopy, AFM | nm – µm | Online/offline |
| | Coating thickness | | | | | Laser triangulation, laser, caliper | ±0.5 µm | Online |
| | Weight | | | | | Infrared camera, Beta sensor, X-ray sensor/Photo sensor | ±0.01 mg/$cm^2$ | Online |
| | Adhesion | | | | | Peel test | ±0.05 N/m | Offline |
| | Porosity | | | | | Pycnometer, Hg porosimeter, calculation | ±10% | Offline |
| | Microstructure/ mesostructure | | | | | SEM images | | Offline |
| | Binder distribution | | | | | SEM-EDX | | Offline |

[a] Machine parameters (MP), which are externally controlled inputs [b] Structure parameters (SP), which are resulting or output properties. [c] Criticality for setting and validating the modeling parameters evaluated as: red for high, yellow for intermediate, and blue for low. [d] For the measurability columns, blue: great difficulty, yellow: intermediate difficulty, and red: easily measurable. [e] For accuracy, blue: poorly accurate, yellow: moderately accurate, and red: highly accurate. [f] The measurement can be made in real-time during production (online) or needs to be made separately (offline).

materials is higher than graphite (ca. 4 g/cm$^3$ vs. 2 g/cm$^3$), and the compaction windows have very different scales. Finally, the formulation components quantities, besides the AM (i.e., binder and conductive additive), and the morphology of the particles play an important role in the calendering properties of the electrodes.[127]

The thickness and porosity measured by geometrical means, *i.e.*, measuring the thickness and areal loading of the calendered electrodes, is a parameter that can be accurately measured online by laser triangulation, laser calipers, X-ray β-radiation, and ultrasound.[100] The rest of the calendered electrode properties are usually measured offline, taking samples of the calendered electrodes. Electrode microstructure-related properties such as porosity and pore size distribution can be measured by Hg porosimetry.[127] In addition, an overview of the calendered electrode microstructure can be determined by computed tomography (CT)[128] or microscopy. Other parameters related to the electrode porosity, such as tortuosity, can be measured by EIS and 3D imaging techniques.[129] Measuring the electrode tortuosity can be challenging since it is an output related to electrode microstructure interacting with a transport process that sometimes requires simulation or transport characterization techniques such as EIS.[130] Additional characteristics for calendered electrodes, such as the hardness, the Young modulus, and the fracture toughness, can be measured by micro-indentation. In addition, the roughness and the adhesion can be measured by profilometry and 90° peeling tests, respectively. The accuracy and the time needed to obtain a representative characterization of the calendered electrodes based on all these offline characterization techniques are highly dependent on the homogeneity of the electrodes since it will determine the number of measurements to be performed. Moreover, mercury porosimetry and 90° peeling tests also depend on the sample preparation procedure, as was discussed in the previous section.

Empirical models on the calendering process can describe the achieved coating porosity as a function of process parameters and electrode properties. The Heckel-based model by Meyer *et al.*[131] introduces the compaction factor as a ratio of minimal achievable coating porosity to the initial one and the compaction resistance, which characterizes the compaction effort. Both decline linearly with rising roll temperatures due to a thermally induced increase in elastic deformability for electrodes containing the thermoplastic binder PVDF. The compaction resistance has a positive linear correlation with mass loading as more contact points increase the overall friction force between the particles. Eventually, the achieved coating density can be described as a function of the line load, the compaction factor, and the compaction resistance.[127,131,132] Usually, the compaction process is controlled by the gap width of the calendaring roles. However, the real gap deviates from the specified value due to roll displacement, depending on the individual calendar and the processed electrodes. It was shown that the detected roll displacement correlates directly and linear to the applied line load and is, therefore, predictable. Additionally, roll displacement enables the determination of the electrode spring-back, which describes the recovery of the electrode thickness directly after the compaction process. The spring-back increases linearly with the applied line load and decreases with higher mass loadings and higher binder weight contents, which induce higher plasticity.[133]

Discrete models can explicitly consider MPs such as gap, pressure, speed, and temperature. In contrast, the accuracy and capability of the models to represent structure parameters can vary. Final thickness, pore network parameters, tortuosity, and mechanical properties are fairly well described, while fracture toughness and roughness could also, in principle, be modeled, albeit with a great computational cost, due to the need for a large domain size. Cohesion between the electrode and current collector is considered but requires some parametrization.

ML models appear efficient for analyzing calendered electrode properties (porosity, thickness, tortuosity, conductivity), directly interlinked with the final electrode performances.[47] Once an ML model takes the standard calendering gap, speed, and temperature as input values, the same model enables the prediction of the associated electrode properties, avoiding the experimental measurements of this manufacturing step. More precisely, the combination of manufacturing parameters from previous steps and the ones detailed above reveals the interdependencies along the fabrication process relevant for the calendered electrode optimization. Table 8 summarizes the experimental and model parameters involved in the calendaring step.

#### *4.1.5. Slitting and post-drying of electrodes*

Slitting is a stage of the roll-to-roll operation to prescribe the electrode width after calendering. It is a low-cost, high-throughput process (80–150 m/min). The conventional slitting machine usually uses a blade or chisel, depending on the electrode type and shape.[12] One of the key points at this stage is the slitting quality of the electrode edges and the cleanliness of the film strip. The slit width of the resultant coils can vary depending on the cell design and the application, which is between 60 and 300 mm.[134] Laser-based cutting techniques are being developed as alternatives to the mechanical cutting process. This technology offers greater flexibility. However, active material damage or contamination through dust increases when laser cutting is used.

Post-drying aims to ensure an electrochemically harmless residual moisture in the low ppm range in the material so that no unwanted gases develop from the chemical reactions that occur after the addition of the electrolyte. Cell manufacturing is produced with dryers connected in a continuous process. Current drying technology typically places electrodes in a low-pressure environment and heating temperatures of 60–150 °C for more than 12 hours with an inert gas supply. However, lower humidity does not always lead to better electrochemistry and mechanical properties. Long-term high-temperature drying could impair the adhesion strength of the PVDF and CMC/SBR binder, damaging the electrode structure.[135] Therefore, the argon purge method can replace vacuum drying, improving

**Table 8.** Summary of the parameters relevant to the calendering step.

| Calendering | | Importance (criticality)[c] Empirical | Continuum | Discrete | ML | Measurability[d] | Accuracy[e] | Online/ Offline[f] |
|---|---|---|---|---|---|---|---|---|
| MP[a] | Gap | | N/A | | | Control | µm | Online |
| | Pressure | | | | | Pressure sensors | | Online |
| | Speed | | | | | Control | | Online |
| | Temperature | N/A | | | N/A | Control | | Online |
| | Electrode composition | N/A | | | | | | Offline |
| | Thickness | N/A | | N/A | | Vernier caliper | µm | Online |
| SP[b] | Porosity | | | | | Calculation, porosimetry, CT | | Online/ Offline |
| | Pore size distribution | | | | | Porosimetry, CT | | Offline |
| | Meso/microstructure | | | | | Microscopy, CT | | Offline |
| | Tortuosity factor *vs.* thickness | | | | | EIS | | Offline |
| | Cross plane tortuosity factors | | | | | 3D imaging techniques, EIS | | Offline |
| | Hardness | | | | | Micro-indentation | | Offline |
| | Young modulus | | | | | Micro-indentation | | Offline |
| | Fracture toughness | | | | | Micro-indentation, microscopy | | Offline |
| | Roughness | | | | | Microscopy, profilometry | | Offline |
| | Adhesion | | | | Peel test | Peel Test at 90° | N/m | Offline |

[a] Machine parameters (MP), which are externally controlled inputs [b] Structure parameters (SP), which are resulting or output properties. [c] Criticality for setting and validating the modeling parameters evaluated as: red for high, yellow for intermediate, and blue for low. [d] For the measurability columns, blue: great difficulty, yellow: intermediate difficulty, and red: easily measurable. [e] For accuracy, blue: poorly accurate, yellow: moderately accurate, and red: highly accurate. [f] The measurement can be made in real-time during production (online) or needs to be made separately (offline).

performance and decreasing energy consumption. It has also been found that a relatively low moisture level (326 ppm with argon purge) could already achieve good electrochemical performance. The small amount of water can improve the formation and stability of the SEI layer in the anode.[136] A widely used technique for measuring moisture is indirect coulometric Karl-Fischer Titration. The accuracy and measurability of this technique can be hindered because the different variables and methodologies used are not precisely detailed and standard, questioning the comparison among results.[137] Therefore, controlling temperature, pressure, and time is essential to have an optimal electrode before assembly.

Empirical models for post-drying focus on the sorption equilibrium of water in electrodes, i.e., residual humidity. Temperature and dew point, combined with activity or relative humidity, are the predominant process and machine parameters, affecting the residual moisture in the electrodes. In addition, the binder system strongly influences the water uptake of the electrode, specially carboxymethyl cellulose (CMC), which is used in water-based solvents. This binder absorbs high amounts of water compared to the remaining electrode materials and thus must be characterized sufficiently. Besides, multiple structural parameters of the electrodes affect post-drying. The porosity is highly critical as it determines the available diffusion volume of the gas phase, which either accelerates or decelerates mass transport. In addition, the electrode pore size is approximated by discrete values instead of using continuous values and standard deviation to reduce the complexity of the models. These discrete values are parametrized based on empirical data. Finally, the tortuosity is modeled by different surrogates, usually as a function of the porosity (e.g., Bruggeman relation).[138,139] Table 9 summarizes the experimental and model parameters involved in the slitting and second drying steps.

#### *4.1.6. Cell assembly*

The separation process is the first step of assembling the pouch cell. During the separation process, electrode cutting is initially carried out with a punching tool or shear cutting, and the electrodes are separated from material rolls. Besides mechanical cutting, laser cutting is becoming more and more popular for cell assembly due to its inherent advantage (i.e., lack of contact), which brings a stress-free separation and thus contributes to the improvement of cell quality.[140]

In a subsequent step, the separated electrode sheets are stacked in a certain order of anode, separator, cathode, separator, and so forth to form a stack. The electrode sheets are usually transported and positioned by vacuum grippers. The positioning of the sheets has been widely recognized as a core quality criterion. However, it is difficult to prevent certain types of defects or faults, e.g., inaccurate positioning, rough cutting edges, and metal dust left on the surface of the electrode sheet, which affects the battery performance and lifespan. Additional machine input parameters are separator tension and stacking speed, directly influencing the achievable stacking accuracy.

The quality of the weld between battery current collector foils and tabs is directly affected by the machine parameters of the welding apparatus. It may vary depending on the deployed technique. Here X-ray techniques detect voids within the weld and thereby ensure good conductivity of the bond.

During the cell assembly, the water content in the air is especially critical to avoiding re-introducing water into the battery materials after drying. Cell assembly operates in dry and clean rooms, where oxygen is present, and the foreign particle content in the air is tracked. The water content in the air is quantified by dew point or ppm measurement. Different sensors can measure dew point with accuracy down to about 2 C[141] and 1 ppm $\pm$ 5 %[142] for the respective techniques. In

**Table 9.** Summary of the parameters relevant to the slitting and second drying steps.

| Slitting | | Importance (criticality)[d] Empirical | Continuum | Discrete | Measurability[e] | Accuracy[f] | Online/ Offline[g] |
|---|---|---|---|---|---|---|---|
| MP[a] | Slitting speed | N/A | | | Control Parameter | ±150 µm to ±250 µm | Online |
| | Pressure | | | | Control Parameter | mbar | Online |
| | Temperature | | | | Control parameter. | °C or K | Online |
| | Porosity, turtousity, PSD | | | | Pycnometer, Hg porosimeter, calculation | nm or percentage | Offline |
| | Time | | | | Control Parameter | min | Online |
| SP[b] | Residual humidity | N/A | | | coulometrischen Karl-Fischer-Titration | ppm | Online |
| | weight | | | | Balance | g | Online |
| Post drying | | Importance (criticality) Empirical | Continuum | Discrete | Measurability | Accuracy | Online/ Offline |
| PP[c] | Binder system | | N/A | | | | |
| | Dew point | | | | Thermo-hygrometer | 1% RH | |
| | Temperature | | | | Control parameter | °C or K | Online |
| | Time | | | | Control Parameter | min | Online |
| | Porosity | | | | Pycnometer, Hg porosimeter, calculation | % | Online |
| | Pore size | | | | | nm | |
| SP | Tortuosity | | N/A | | Picnometer, Hg porosimeter, calculation | nm or percentage | Offline |
| | Residual moisture | | | | | | Online and Offline |

[a] Machine parameters (MP), which are externally controlled inputs. [b] Structure parameters (SP), which are resulting or output properties. [c] Process parameters (PP), which cannot be controlled externally but are the result of the chosen MP, and they have an effect on the result of each step. [d] Criticality for setting and validating the modeling parameters evaluated as: red for high, yellow for intermediate, and blue for low. [e] For the measurability columns, blue: great difficulty, yellow: intermediate difficulty, and red: easily measurable. [f] For accuracy, blue: poorly accurate, yellow: moderately accurate, and red: highly accurate. [g] The measurement can be made in real-time during production (online) or needs to be made separately (offline).

some instances, the lab-scale cell assembly is performed under an inert gas atmosphere, where the oxygen content is strictly controlled (1 ppm ± 2%).[143] Overall, the atmospheric conditions are well measurable, with high accuracy, and online during the manufacturing plant operation.

Due to the numerous processing parameters involved in the assembly process, it is rather challenging to build a deterministic model for the assembly process to predict quality parameters such as stacking accuracy. A more appropriate approach is to monitor the assembly process directly. In the case of defect detection, for example, the electrode surface defects can be identified by using a camera. Based on monitoring data, a model-driven approach can be built to replace the labor and automate tasks such as defect identification. In a broad sense, we consider this model-driven monitoring approach as a member of ML models.

The stacking error is an important quality criterion to estimate the packaging failure. Within empirical models, it is correlated with cell performance. It is possible to assess a maximum tolerance for the stacking process that does not negatively influence battery cell quality. Cell stacking (z-folding) results in a multitude of anode-separator-cathode-separator compartments. By considering the worst-case scenario, i.e., the maximum placement error for each handling process, Schmitt and Raatz built a simulation approach to predict the rotational/translational positioning error and the overlap for every single stacking.[72] This model uses the size of electrodes and the number of electrodes to be stacked as input data, coupled with a normal distribution for the deviation of the stacking determined by the assembly process. The idea is to use random numbers generated from the normal distribution to represent the error of the stacking process.

Conventional Computer Vision (CV) methods have been widely used in industrial defect detection with low computational cost. The input data can be ordinary 2D pictures, radiographic images, or 3D CT reconstructions. Classical algorithms such as the Canny edge detector[144] and Hough transformation[145] have already enabled high-precision online monitoring in edge recognition and blur detection.[146] However, feature extraction and task objectives are built separately within the traditional CV framework. The main challenge for the CV is to extract the features of the image. The accuracy and reliability of the CV models depend directly on the handcrafted features and the methods used for feature extraction. Choosing a set of features based on experience alone is almost impossible if the image clarity diminishes or the image becomes increasingly complex.

With the development and maturity of AI and CV technology, photos from different stages of the stacking process, *e.g.*, pickup and placement of electrodes or overfolding of the separator, can be analyzed in-depth. With the help of deep learning and transfer learning,[147] it is now possible to automatically detect defects in the micro and macrostructure from images of the sectioned cells. Several papers have reported over 97%[147,148] defect detection accuracy, which is well beyond the best results of the manual inspection with human eyes. Agglomerates can be detected close to a diameter of 0.5 mm. CV allows the detection of foreign particles, *e.g.*, metal particles, down to a diameter of 40 µm. Cracks can be identified down to a similar size. The accuracy for both is around 20 µm. The machine vision software Halcon developed

by MVTec meets most defect detection requirements in battery production.

X-ray is typically used for the non-destructive test (NDT) of online battery cell defects after the process steps of stacking, welding, and enclosing in the automotive and aviation industry. The methods employed in production up-to-date rely on the purely two-dimensional radiographic images of the battery stack. In contrast, the methods available at the laboratory scale can rely on three-dimensional CT since the acquisition, and image analysis are not as time-critical. A test process may last two to four seconds in a pilot line environment. One second test time will be the target value for the next NDT generation systems. Several X-ray tubes and detector assemblies are operating in parallel to perform rapid testing, each for a specific section of the battery cell, e.g., the corners, edges, and the center, involving up to six assemblies to screen a single battery cell. Thereby, the detection of different stacking defects is ensured. The sheets in a battery cell are tested regarding anode-cathode-overlap, offset, tilt and rotation. Given the latest design with thinner and more layers, conventional 2D inspections are coming to their limits in detecting these faults safely.

Additionally, manufacturers wish to check the stack for metallic particle contamination by X-ray besides optical means. The target is to find copper, nickel, or aluminum particles, with sizes typically between 30 and 50 μm, down to 20 μm in the future. Today, only high-end 2D/3D offline systems can detect those metals, seeking online detection in the future. X-ray is further used to estimate the quality of the weld between current collector tabs and electrode tabs. Here, the porosity of the weld is especially of interest. Challenging requirements for a lower false reject rate are Increasingly driving the demand for developed resolution systems that should achieve shorter test times and lead to a market introduction of (quasi) 3D X-ray imaging. As for all online X-ray applications, defects need to be found and classified by automatic defect recognition software, which is well established in the 2D domain but will need further algorithm development in 3D image analysis. AI-based analyzing tools will be valuable add-ons to conventional imaging analytics tools. New image chain developments are required to further increase the speed of 3D inspection technologies. Another challenge will be to create an efficient way to handle the massive amount of X-ray imaging data produced from current/future digital twins and pilot lines to detect defects and electrode organization. X-ray data can be seen and developed as an ultimate cell data sensor, leading to immediate process control feedback loops for digital twins and pilot lines. Table 10 summarizes the experimental and model parameters involved in the cell assembly step.

#### *4.1.7. Electrolyte filling*

The process step of electrolyte filling is the final step of cell assembly, in which the cell stack materials are combined with the electrolyte to form an electrochemically active unit. It includes the transition to the cell finish and can be divided into filling and wetting. The filling is when the electrolyte is filled

**Table 10.** Summary of the parameters relevant to the cell assembly step.

| Cell assembly | | Importance (criticality)[c] Empirical | Continuum | Discrete | Measurability[d] | Accuracy[e] | Online/ Offline[f] |
|---|---|---|---|---|---|---|---|
| PP[a] | Separator tension | | N/A | | | | Online |
| | Stacking speed | | | | | | Online |
| | Atmosphere parameters ($H_2O$, $O_2$, foreign particle content) | | | | Thermo-hygrometer | 1 % RH | Online |
| SP[b] | Contact welding parameters, depending on the method | N/A | N/A | N/A | | | Online |
| | Stacking/winding overlap | | | | Camera, X-ray | ±100 μm | Online/ Offline |
| | SA: offset | | | | Camera, X-ray | ±100 μm | Online/ Offline |
| | SA: tilt/rotation | | | | Camera, X-ray | ±100 μm | Online/ Offline |
| | Metallic particle contamination | | | | Camera, X-ray | 30–50 μm particle size, 20 μm perspective | Online/ Offline |
| | Stack weight | | | | Balance | | Online |
| SP | Area with opposing counterpart | | N/A | | The capacitance of the dry cell | | Offline |
| | Defects on electrodes | | | | Camera (limited resolution, no microscopic defects) | cm–mm | Offline |
| | Defects on separator | | | | Camera (limited resolution, no microscopic defects) | cm–mm | Offline |
| | Contact weld quality | | | | X-ray (porosity), electrical resistance | | |

[a] Process parameters (PP), which cannot be controlled externally but are the result of the chosen MP, and they have an effect on the result of each step. [b] Structure parameters (SP), which are resulting or output properties. [c] Criticality for setting and validating the modeling parameters evaluated as: red for high, yellow for intermediate, and blue for low. [d] For the measurability columns, blue: great difficulty, yellow: intermediate difficulty, and red: easily measurable. [e] For accuracy, blue: poorly accurate, yellow: moderately accurate, and red: highly accurate. [f] The measurement can be made in real-time during production (online) or needs to be made separately (offline).

into the cell before being sealed from its environment. After the pores of the cell stack material are filled with the injected electrolyte, this process is called wetting, where the main driver is the capillary forces acting against the remaining gas in the pores.

The electrolyte filling step differs depending on the cell housing type. While pouch cells have a larger dead volume due to their soft case enclosure, prismatic or round cells often require several filling steps with waiting times due to their rigid hard case housing to fill the required amount of electrolyte into the cell. Thus, it becomes apparent that the filling and wetting times cannot be distinguished with any degree of separation since a certain amount of wetting is required for complete filling.

The process step aims to achieve sufficient wetting of all porous cell stack materials so that a uniform ion flow occurs in the subsequent formation without impairing the electrochemical performance. From a production engineering point of view, the wetting time should be as short as possible in terms of waiting time and the highest possible throughput.

The process step of electrolyte filling is characterized by many product and process parameters that influence each other. The quantity of electrolyte and the chamber pressure or pressure profile is decisive for filling. The minimum electrolyte volume is defined by the volume of pores present in the cell stack materials. For NMC111 electrodes, a factor of 1.4 times the pore volume has been shown to be optimal for electrochemical performance. In his work, Günter shows that the initial capacitance achieved after forming and the cycling stability after 500 cycles is best for volume factor 1.4, and the researchers support this statement with further electrochemical investigations such as electrochemical impedance spectra.[149] During filling and before closing the cell, the chamber pressure should be kept as low as possible to reduce the amount of gas in the pores and thus keep the difference between capillary pressure and gas pressure as large as possible.[150] A lower limit for the minimum chamber pressure is the saturation vapor pressure of the electrolyte, where, if it falls below, evaporation will occur. Thus, the amount of electrolyte will be reduced.[151] The last parameter listed is the dosing speed and cycles. This is controlled by pressurization of the electrolyte, although some electrolytes tend to foam due to excessive dosing pressures.[152] Variation and optimization of the filling parameters improve the electrochemical performance or reduce the wetting time.

During wetting, the temperature, in particular, is a major influencing factor. Thus, the wetting rate increases as a result of improved wetting properties of the electrolyte (viscosity, surface tension, and density) when the storage temperature is increased.[153,154] Besides, a limiting factor at the storage temperature is the decomposition/degradation of the electrolyte, resulting in a deterioration of the electrochemical performance. A linear load in the form of cylindrical rolls can be used to homogenize and improve the macroscopic distribution of the electrolyte in the cell. In addition to the influencing factors on the process side, the wetting properties of the cell stack materials used on the product side are highly relevant. The upstream production processes determine these in electrode and cell manufacturing. Calendering of the electrodes increases volumetric energy density by compressing the pore system. This shift in pore size distribution to smaller pores leads to a degradation of wetting properties and an increase in the required wetting time.[155] Similarly, the choice of separator material and its coating has a major impact on the wetting properties of the entire cell stack.[156] While the conventionally used poly elipse separators made of PE and PP wetted poorly with the hydrocarbon solvents, creating a bottleneck in the joint wetting,[157] coatings with ceramic particles or with PVDF improve the surface energy so that the material-specific wetting properties of the separators are comparable to those of the electrodes.[158,159] Furthermore, additional process steps during cell production, such as lamination of electrodes and separators[160] or laser structuring of the electrodes[150] improve the wetting properties of the cell materials and thus lead to faster wetting of the entire cell.

In order to quantify the wetting time, the degree of wetting, *i.e.*, the proportion of wetted cell material pores, is measured. Different offline approaches are available for this purpose that need further experimental preparation, challenging the measurability and accuracy. Since the cell materials are in non-transparent cell housings made of aluminum at the time of filling, optical inspection of the degree of wetting is only possible using radiographic methods. While neutron radiography can show the hydrogen components of the electrolyte with time and spatial resolution.[161] X-ray radiation provides an image of the movement and distribution of the contrast agent dissolved in the electrolyte. Visualization without a contrast agent is a subject of current research. In both methods, the wetting fronts of the electrolyte and, thus, the wetted areas can be displayed arithmetically averaged over the cell thickness in a two-dimensional image. Likewise, statements about the wetting quality, such as the formation and distribution of bubbles of the residual gas, are possible. Another methodology is electrochemical impedance spectroscopy, in which the AC resistance is measured. Due to the lack of formation, the resulting impedance spectra do not correspond to the known semicircular spectra. However, a conclusion on the degree of wetting can be drawn from the temporal change of the spectra. Possible evaluation criteria can be the high-frequency resistance at an imaginary part of 0 ohm[162] or the resulting impedance at a frequency of 1 Hz.[160] Over time, both resistances decrease due to the increasingly wetted area.

As another method, research is being conducted on ultrasonic sensors that can provide information on the degree of wetting due to the different transmission properties of non-wetted (pores filled with gas) and wetted (pores filled with electrolyte) areas.[163] Furthermore, it is also possible to show the degree of wetting with the aid of thermography.[157]

Continuum and discrete models focus on the wetting rather than the filling as they are mostly concerned with micrometer scale phenomena. An empirical model dealing with the influence of evacuation pressure and temperature comes from Günter *et al.*[153] The authors used a model based on a full linear momentum balance of liquid in an inclined tube to describe the liquid transport and thus also the degree of wetting within

porous cell material. The effects of both residual gas and gravity are taken into account. The validation of the model was done by experiments on Hardcase and Pouch cells.

As explained in Section 3.2.4., LBM is a discrete model that has been used to model the flow of electrolyte within the pore network of electrodes individually and in full cells (wetting).[52,164] This accurate technique is limited in domain sizes and cannot currently describe a real-sized system. The main inputs for these models are related to the identity of the electrolyte (viscosity, density), the solid/fluid interaction (contact angle, type of collision operator), the inlet pressure, and the structure acting as the simulation domain. The output is the electrolyte and air densities at each point within the pores as a function of time, from which a saturation curve can be obtained. Temperature is a critical parameter to consider indirectly, as it affects viscosity, density, and contact angle. Dosing, dosing speed, pressure, and press rolling parameters are all grouped in the external pressure, used as a boundary condition. This parameter can be fixed or considered as a function of time. The wetting time can be easily considered from the saturation curves, closely related to the wetting degree, which is explicitly obtained as output. The final state of the simulation can be used for subsequent electrochemical simulations to evaluate the electrical function, albeit with an additional high computational cost.[52]

ML models are a relevant tool to bypass the high computational cost LBM simulations.[53] The analysis of the electrolyte infiltration along time appears as the most critical output of the ML models, where the 3D mesostructure can be directly embedded as the input of the model. We extract the pore-network configuration from such a 3D volume to evaluate the meaningful features describing the mesostructure and then calculate the infiltration without launching the LBM simulation. Table 11 summarizes the experimental and model parameters involved in electrolyte filling and wetting steps.

The step that immediately follows electrolyte infiltration is the sealing of pouch cells or soldering in cylindrical cells. To the best of our knowledge, no models have been reported to describe these processes. This indicates a notable opportunity for future research. Sealing of pouch cells is a very elementary process when it comes to cell quality and lifetime. It is carried out by hot bars or heated resistances. In terms of characterization, the critical parameters of this process are pressure, time and temperature.[165] A good seal is necessary to ensure long calendar life,[166] since it limits gas and moisture permeation. However process control is quite easy when the parameters have been determined. In terms of tests, the pouch cells are checked with X-ray radiography for any foreign particles and alignment issues. The seals can also be inspected visually to find wrinkles or other defects. To estimate the sealing quality and tightness, a megger test can be performed.[167] Lastly, the impedance between the anode and a probe such as a conductive brush (e.g., copper wire) on top of the pouch foil can also be used to detect any openings in the sealing.

#### 4.1.8. Formation process and degassing

The formation process is important for battery manufacturing because of the high cost and time demand and the tight relationship with battery degradation and safety issues. Forming refers to the initial processes of charging and discharging the battery cell. Subsequently, the cells are guided into special carriers in form stands and brought into contact with them by spring-loaded contact pins. During the formation process, lithium ions are intercalated in the crystalline structure of the graphite on the anode side. Electrolytes used in LIBs consisting mainly of carbonates solvents are not stable below around 0.8 V vs. $Li^+$ and are reduced on the surface of graphite. This creates the solid electrolyte interface (SEI), a boundary layer between the electrolyte and the electrode. At this step, gaseous

**Table 11.** Summary of the parameters relevant to the electrolyte filling and wetting steps.

| Electrolyte filling and wetting | | Importance (criticality)[c] | | | | Measurability[d] | Accuracy[e] | Online/ Offline[f] |
|---|---|---|---|---|---|---|---|---|
| | | Empirical | Continuum | Discrete | ML | | | |
| MP[a] | Electrolyte quantity (filling) | | | | | Machine parameter | | Online |
| | Temperature (filling) | | | | | | | Online |
| | Dosing speed and cycles (filling) | | | | | Machine parameter | | Online |
| | Chamber pressure profile (filling) | | | | | Machine parameter | | Online |
| | Temperature (wetting) | N/A | | | | | | Online |
| | Pressure profile (wetting) | | | | | N/A | N/A | Online |
| | Press rolling parameters (wetting) | | | | | | | Online |
| | Wetting time | N/A | | N/A | | | | Online |
| SP[b] | Wetting degree | | | | | EIS, HFR, charge transfer, Ultrasound; X-Ray/neutron CT/radiography | | Offline |
| | Electrical function | | | | | OCP, EIS, Test for Shorts | | Offline |

[a] Machine parameters (MP), which are externally controlled inputs. [b] Structure parameters (SP), which are resulting or output properties. [c] Criticality for setting and validating the modeling parameters evaluated as: red for high, yellow for intermediate, and blue for low. [d] For the measurability columns, blue: great difficulty, yellow: intermediate difficulty, and red: easily measurable. [e] For accuracy, blue: poorly accurate, yellow: moderately accurate, and red: highly accurate. [f] The measurement can be made in real-time during production (online) or needs to be made separately (offline).

byproducts are formed. The parameters during formation vary depending on the cell manufacturer and significantly impact the cell's performance. They depend on both the cell concept, targeted application, and cell chemistry and represent the basic knowledge of a cell manufacturer.

In some cases, the cells in the particular bag are pressurized by special product carriers applied during the forming process. First charges are normally carried out between 0.1 C and 0.5 C, and a state of charge (SOC) of approximately 20% to 80%. The duration of the charging process can be up to 24 hours. These slow formation steps can significantly increase the cost of capital investment and consume more labor and space resources.

In addition to the electrochemical activation conditions, the temperature is another important parameter to consider during the forming process. Increasing the ambient temperature leads to faster formation processes and lower cell internal resistance. Higher temperatures can increase the conductivity of the electrolyte through the separator, improve the diffusivity of solids in the AM particles and reduce the resistance to charge transfer at the electrode-electrolyte interface. But it also leads to the formation of an unstable SEI layer due to electrolyte degradation. The appropriate temperature conditions are still unclear. Therefore, it is necessary to record the temperature during the formation process for its subsequent relation to the final performance of the battery.

At some point during formation, when SEI has been formed, and gas evolution is complete, a degassing step is applied in the case of pouch cells since this format cannot tolerate internal pressure. On the other hand, for cylindrical cells like 18650, gassing results in internal pressure build-up without consequence on the dimension of the cell, so degassing is not mandatory. In the case of hard casing prismatic cells, cells can be degassed or not depending on mechanical design and gas volume produced during formation.

For this reason, the degassing process has been of great interest to the scientific community for some years now. Recently, methods have been developed to determine the volume, pressure, and identification of the gases generated during the formation process.

The simplest method to monitor the gas evolution is the measurement of the thickness of the cells in the pouch cell. The variation of the cell thickness should provide information on the degree of gas evolution or the consumption of lithium-ion batteries. However, this inaccurately assumes that the expansion is uniform throughout the cell.[168] Archimedes' principle has been used to devise a method of monitoring cell volume during operation and provides a more accurate representation of the amount of gas evolution.[169,170] Although these methods give information about the extent of gassing, they do not give information about the composition of the gases. Gas chromatography and mass spectrometry are techniques being developed to identify these gases.[171–173] Mass spectrometry has the greatest potential application in the industry due to its ability to perform online measurements.

Quality control is an integral part of the manufacturing process. It is usually done at the end of the manufacturing line by measuring the self-discharge after a long period (after weeks). Abnormal voltage drop and short circuit may indicate defects arising from electrode misalignment, separator defect, or foreign particles in the cell. Resistance and capacity measurement may also be analyzed after electrical formation. Additional tests include end-of-line testing, which is done by performing pulse tests, internal resistance measurements (DC), optical inspections, OCV tests, and leakage tests.[174,175]

One can define empirical functions relating the electrochemical parameters and chamber temperature with the cell capacity and internal resistance.

Continuum models based on the Newman approach typically consider electrochemical parameters to predict the SEI thickness evolution.[60,176,177]

A similar situation is for discrete models based on the kinetic Monte Carlo approach reported in the literature.[178,179]

ML models have been used to correlate electrochemical parameters with SEI formation in a few ways: generate ML potentials for MD simulations, predict electrode density, or predict reaction networks.[180] They are also considered useful in scale bridging for multiscale simulations and generating microstructure-electrochemical property correlations through variational autoencoders or generative adversarial networks.[180] Table 12 summarizes the experimental and model parameters involved in the formation and degassing steps.

### 4.2. Data management solutions (software)

For modeling (mechanistic and data-driven), desired data needs to be acquired from various data sources characterizing relevant information concerning production processes and products. This data needs to be allocated to the corresponding entities (e.g., intermediate products, structures, process steps, production lots) to establish a relation between the physical world of battery production and the acquired data. Finally, the data can be stored either as raw data or be reduced to only the relevant information and stored as consolidated data after several preprocessing and transformation steps. It is then important to establish access to the data in the data storage for modeling purposes.

In battery cell production, a plethora of different data sources exist process step/production machines, energy carrier meters, technical building services (TBS)/room sensors, intermediate product analytics, final product analytics, and operational data (see Figure 8). These data sources contain data providing different information, e.g., energy demand, intermediate product structures, production times, or ambient conditions. A connection to the physical data access point must be established to acquire data from these sources. These physical data access points are hardware through which the data of the data source can be obtained (e.g., PLC, sensor, measuring device, server). The data can then be acquired through a data acquisition interface. This interface can be communication protocol (e.g., Profinet, OPC UA, Modbus), analog/digital signals, connection to a file (e.g., Excel files, word files, image files), or a database (e.g., SQL, NO-SQL)

Review
doi.org/10.1002/batt.202200224

Chemistry Europe
European Chemical Societies Publishing

**Table 12.** Summary of the parameters relevant to the formation and degassing steps.

| Formation parameter and degassing | | Importance (criticality)[c] | | | | Measurability[d] | Accuracy[e] | Online/ Offline[f] |
|---|---|---|---|---|---|---|---|---|
| | | Empirical | Continuum | Discrete | ML | | | |
| MP[a] | Electrochemical parameters (current, Voltage, time.) | | | | | Formation bench, Control battery system | µA or mV | Online |
| | Chamber Temperature | | | | | *Tc*, IR sensor | °C | Online |
| | External mechanical pressure | N/A | | | | Pressure sensor, dynamometric wrench | MPa | Online/ |
| SP[b] | Capacities (ch. /discharge) | | | | | Control battery system | mAh/g | Online |
| | Coulombic efficiency | N/A | | N/A | | Calculation | Percentage | Online |
| | Energy efficiency | | | | | Calculation | Percentage | Online |
| | Initial capacity loss | | | | | Calculation | | Online |
| | Initial irreversible thickness increase | | | | | | µm | Online |
| | Internal resistance | | | | | EIS, DC pulse | mOhm | Online |
| | Quality control | N/A | | | | Voltmeter | | Online |
| | Degassing: gas volume and composition | | | | | Archimedes, GC/MS | µL/ppm, %/nmol | Offline/ online |
| | Hard casing cells: internal pressure | | | | | Gas pressure sensor | | Offline |

[a] Machine parameters (MP), which are externally controlled inputs. [b] Structure parameters (SP), which are resulting or output properties. [c] Criticality for setting and validating the modeling parameters evaluated as: red for high, yellow for intermediate, and blue for low. [d] For the measurability columns, blue: great difficulty, yellow: intermediate difficulty, and red: easily measurable. [e] For accuracy, blue: poorly accurate, yellow: moderately accurate, and red: highly accurate. [f] The measurement can be made in real-time during production (online) or needs to be made separately (offline).

connection. The acquired data can be of different formats, such as time series, spatial, and discrete data, and can be available either live or as stored historical data. Many sensors and analytical devices can additionally be distinguished between being in-line or offline concerning the production line.

In-depth data analytics or modeling approaches require large amounts of data to exploit their fullest potential. Due to the previously discussed complexity of the battery production process and the manifold of different data sources, traceability becomes more important to gather as much data as possible and supply sufficient information (i.e., batch vs. instance level). Traceability is defined as "the ability to trace the history, application or location of an object".[183] In the past, traceability systems were used when handling recall campaigns in different industries. In the context of battery cell production, recalls are still important, but since quality management (*e*, VQG) is becoming more relevant due to the high environmental (e.g., scrape rates, energy consumption) and economic/political (costs, regulations) impact of the battery production process, transparency along the process chain and product-specific data is essential.

The key function and the role of traceability within production environments are shown in Figure 9. Traceability embodies two core elements: (1) trace and (2) track.[184] Tracing describes an upstream process of recreating or extracting a specific object's product and process history (i.e., trace-object) in an interlinked and consistent data set. Tracking is the downstream process and embeds the function of identification and linkage of the trace object to a unique ID and the information recording and saving.[185] As battery production covers batch (or semi-contentious) and single-unit processes with converging and diverging material flow, identifying the "right" trace object and equipping it with an identification technology (e.g., QR-code, RFID-chip) without influencing the perceived quality of the product is under ongoing research. Solutions and technology suggestions for different identification approaches have been discussed and presented in.[186–188] Next to the object identification through ID, the detection of production stages through energy monitoring can support the often manual tracking process.

The functions of the information recording and sharing within a traceability system for battery production are challenging, i.e., due to heterogeneous data distribution and the large volume, which leads to incompatibility of applications relying on its functionality. To encounter this, ontology-based systems can support better integration of specific domain knowledge and thereby improve the interoperability of applications, new data integration, and improved data quality.[188]

OpenSemanticLab[189] is an initiative to build an ontology-ready end-to-end data and knowledge management solution based on OpenSource web services. MediaWiki provides the core document and file storage with extensive interfaces for humans (editors) and machines (APIs). Templates and forms ensure uniformity and efficiency. The extension Semantic MediaWiki provides the Wiki with numerous possibilities for linking and annotating data. In addition, semantic queries can be sent directly to the Wiki or its SPARQL endpoint, and results can be visualized in various ways. The core (meta) data structure is flanked by a time series database specialized in continuous data acquisition. Such data streams can be transmitted from the laboratory using Node-RED, especially from OPC-UA capable devices. Finally, users can access via JupyterLab all data stored in the system, process it, and push the results back. The project is currently under heavy development and is planned to get released within the next month. Some of the results are already being used in a nationally-funded project.[190]

| Data Sources | Data Description | Data Access Point | Data Acquisition Interface | Data Format |
|---|---|---|---|---|
| **Process Step/ Production Machine** | Process Parameters State Variables | PLC | Communication Protocol (PROFINET, OPC UA, Modbus, PROFIBUS, etc.) | Time Series |
| **Energy Carrier Metering** | Energy Demand | Sensor | Analogue/ Digital Outputs | Time Series |
| | | Measuring Device | Communication Protocol | |
| **TBS/ Room Sensors** | Ambient Conditions | PLC | Communication Protocol | Time Series |
| | | Sensor | Analogue/ Digital Outputs | |
| **Intermediate Product Analytics** | Intermediate Product Features (IPF) | Sensor | Analogue/ Digital Outputs | Times Series, Distribution, Spatial, Discrete Data |
| | | Analytical Device | Communication Protocol or Data File System (File) | |
| **Final Product Analytics** | Final Product Properties (FPP) | Analytical Device | Database (Query) | Time Series & Discrete Data |
| | | | Data File System | |
| **Operational Data** | Production Times Material Amount ... | Production Plan | Communication Protocol or Database (Query) | Discrete Data |
| | | | Spreadsheets or Data File System (File) | |

**Figure 8.** Exemplary data sources in LIB production and relevant information for data acquisition. Adapted with permission from Refs. [181,182] Copyright (2020) Wiley-VCH.

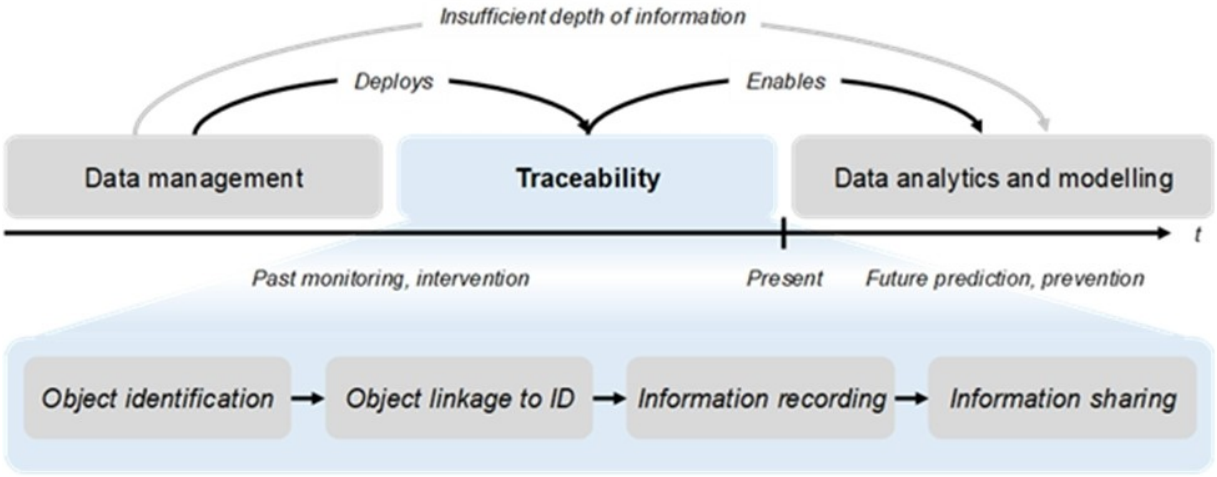


**Figure 9.** Functions of a traceability system. Adapted with permission from Ref. [182] Copyright (2020) Elsevier.

An example of a European project where data management and storage are crucial is the BIG MAP project.[191] This project deals with developing an AI-orchestrated infrastructure capable of optimizing SEI and Cathode Electrolyte Interphases in LIBs. The project combines multiple experimental and computational modeling efforts to collect data used for the AI. Therefore, it becomes crucial to harmonize data, ease its searchability, and ensure interoperability. Software technologies are being developed for that purpose (Figure 10).

For example, the Battery Interface Ontology (BattINFO) is a battery chemistry ontology based on the top-level European Materials and Modelling Ontology (EMMO).[192] BattINFO aims to formalize the current state of knowledge on physical and chemical processes at the inner interfaces. The definitions included in BattINFO are based as much as possible on accepted standards and other reference literature on the subject. The goal is to provide a unified structure to support interoperable data for battery characterization and modeling within the BIG-MAP project.

The Battery Value Chain Ontology (BVCO) is a sister ontology of BattINFO, aiming to ontologize essential parts of the battery value chain.[192,193] BVCO is dedicated to the higher-level process chains for material processing and manufacturing to create a unified structure for process specifications and process-related data. It imports BattINFO (and therefore also EMMO) and applies the basic definition of the battery as a system made there. The BVCO also interacts directly with the General Process Ontology (GPO),[194] which describes terms common across different process engineering domains. The BVCO is being developed under the coordination of Fraunhofer ISC as part of both EU and national research projects. It is hosted in a public repository on GitHub[195] and available for use under a creative commons CC-BY-4.0 license.

In terms of synthetic data from models, one approach for generation is the ARTISTIC project online calculator.[196] This is a freely accessible platform with a user-friendly interface that gives access to 3D manufacturing models. The manufacturing steps currently include the slurry phase, drying, and electrode calendering. It is envisioned to expand these to electrolyte infiltration and electrochemical characterization. Each simulation launched by the users is available to all. Thus, it consists of a continuously growing open-access database that links manufacturing conditions and 3D electrode microstructures.[28]

## 5. Conclusion

The development of digital technologies is required to improve the industrialization of new batteries and shorten the time to market. For instance, the design of ML-supported algorithms will accelerate the discovery of materials and the development of AI-orchestrated characterization of battery materials and battery cells. Combining computer-aided engineering tools and experimental measurements will help understand and predict battery performance. The democratization of such tools and methods will be essential for a competitive industry in Europe.

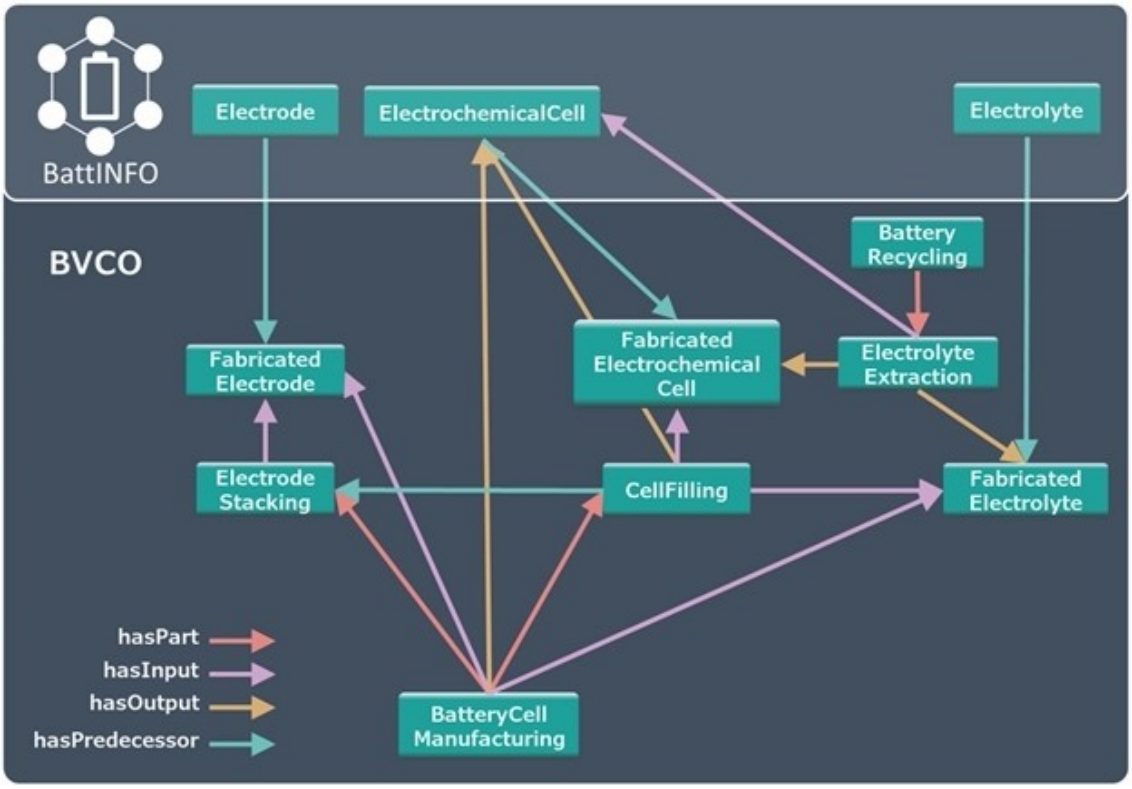


**Figure 10.** BVCO-BattINFO alignment. Reproduced from Ref. [192] (CC BY 4.0).

Digital twins can be used during the discovery, R&D, production, and usage cycles to improve battery performance, lifetime, safety, manufacturability, and recyclability. Methods for big data analytics can be developed and feed the digital twins, while the internet of things-based data analytics can improve the maintenance cycle. The design of experiment methodologies can benefit from digital twins to accelerate the industrialization of new batteries.

After discussing the need for digital twins for battery manufacturing, in this article, we first reviewed some of the ongoing European research efforts on the digitalization of manufacturing processes and key aspects underlying their computational modeling (methodologies currently developed and available software). One can say that computational modeling gives promises to be at the heart of battery manufacturing and engineering. The first step is to make the best use of the available modeling approaches and combine them when possible. The next step is to integrate these available models with other digital technologies, like product lifecycle management, industrial internet of things, manufacturing operations management, and supply chain-related solutions. The integration of modeling tools with such other technologies is already possible. Nonetheless, it highly depends on the motivation of battery laboratories and companies to launch digital transformation programs with an end-to-end integrated digital platform.

Then, we reported a novel classification of LIB manufacturing data types to develop digital twins of prototypinglines. This classification can be seen as a data model or metadata template. It was performed regarding the criticality of developing different process models (based on empirical, continuum, discrete, or ML approaches), the accuracy of the experimental measurements of relevant properties (e.g., coating thickness), and the possibility of not measuring in real-time. Materials science, process engineering, characterization aspects, computational modeling, and data sciences support such classification results from a collaborative transdisciplinary effort. This study identifies several gaps between parameters that can be measured and parameters needed for the development of some of the computational models, such as material storage conditions for the slurry, temperature during electrolyte wetting, or self-discharge after formation. Given the technological progress, one could foresee that it will become possible to measure online some of the parameters that cannot be measured online today, such as PSD or particle morphology during slurry formulation, binder distribution after drying or calendering, or wetting degree after electrolyte infiltration.

Finally, we discuss ways to deal with this type of data, needed hardware and software infrastructures, by mentioning some initiatives towards this.

While the analysis was performed for LIBs, this study is fully transferable to some other battery types (e.g., Sodium-Ion Batteries) where the wet processing approach is used. Additionally, some of the manufacturing stages for the production of different battery technologies are partially transferable from LIB, as detailed in a review by Duffner *et al.*[197] and as such our discussion is also relevant in those cases, particularly for electrolyte filling and SEI formation steps. However, some of these technologies involve significantly different manufacturing steps, and as such will require radically different approaches. For some of these, such as lithium-sulphur battery manufacturing, initial steps have been taken to address these issues,[198] but as these technologies are developed, more work will be required regarding digitalization, accounting for each specific step and technology.

The use of computational software for battery manufacturing at an industrial level is not yet democratized. It relies heavily on the habits of engineers and PhDs and their personal experience with such tools. Still, there is a clear acceleration in the interest in modeling technologies. The community will take some time to adopt them and fully benefit from their capabilities. Ultimately, we envision that computational modeling will be used in the battery manufacturing industry to a larger extent.

We believe that the present work paves the way towards concrete digitalization of battery manufacturing pilot lines and eventually including autonomous processes, which started to emerge in other fields.[199,200] This is because we think that our work provides a solid background to establish practical recipes and a list of good practices and recommendations on how to implement digital twins of battery prototyping lines. It also constitutes a solid background for battery manufacturing data standardization and ontology initiatives such as the ones mentioned in the roadmap of the European Battery 2030+ research program or the ones that could be undertaken in future European projects. Last but not least, it is worth mentioning that several of the data types discussed in our study can also be found in production lines. Therefore, we are confident that this work also provides useful information for the industry. From an industrial perspective, the parameters mentioned above related to the entire manufacturing process are of utmost importance. These parameters are typically measured and controlled to ensure a stable process and, in the end, a safe product for the customers. Enhancing the insights one gets from these parameters through the presented approaches will surely lead to beneficial developments on the production scale, especially for the quality and the reduction of energy consumption throughout the entire process.

## Appendix

The present article is accompanied by an interactive website that allows exploring the information presented in Tables 5 through 12 in an interactive way. This website can be accessed through the following URL: https://www.erc-artistic.eu/fileadmin/user_upload/LiPLANET/index.html.

## *Acnowledgements*

*A.A.F. and D.Z.D acknowledge the European Union's Horizon 2020 research and innovation program for the funding support through the European Research Council (grant agreement*

*772873, "ARTISTIC" project). A.A.F. and F.M.Z. acknowledge the European Union's Horizon 2020 research and innovation program under grant agreement No 957189 (BIG-MAP). A.A.F. acknowledges Institut Universitaire de France for the support. E.A., M.D., and A.A.F. acknowledge the ALISTORE European Research Institute for funding support. E.A., I.B., F.H. and C.B. gratefully acknowledge financial support from the European Union's Horizon 2020 Research and Innovation Programme within the project "DEFACTO" (grant agreement No 875247). The LiPLANET Project has received funding from the European Union's Horizon 2020 Research and Innovation Programme under Grant Agreement N. 875479. C.B. acknowledges support by the Federal Ministry of Education and Research (BMBF) within the Project "Sim4Pro", (grant no 03XP0242A).*

## Conflict of Interest

The authors declare no conflict of interest.

## Data Availability Statement

Data sharing is not applicable to this article as no new data were created or analyzed in this study.

**Keywords:** data standards · digital twin · lithium-ion batteries · manufacturing · metadata

[1] "Strategic Research and Innovation Agenda – BATT4EU," can be found under https://bepassociation.eu/our-work/sria/, **n.d**.
[2] C. Pillot, in *Batter. Conf. Exhib.*, Nice, France, **2019**.
[3] S. Ortiz, I. Careaga, "Gigafactories: Europe's major commitment to economic recovery through the development of battery factories | CIC energiGUNE," can be found under https://cicenergigune.com/en/blog/gigafactories-europe-commitment-economic-recovery-battery-factories, **n.d**.
[4] A. Colthorpe, "Europe to be world's biggest lithium-ion battery cell maker after China by 2025," can be found under https://www.energy-storage.news/europe-to-be-worlds-biggest-lithium-ion-battery-cell-maker-after-china-by-2025/, **2021**.
[5] O. Rynne, M. Dubarry, C. Molson, D. Lepage, A. Prébé, D. Aymé-Perrot, D. Rochefort, M. Dollé, *Batteries* **2019**, *5*, 72.
[6] O. Rynne, M. Dubarry, C. Molson, E. Nicolas, D. Lepage, A. Prébé, D. Aymé-Perrot, D. Rochefort, M. Dollé, *ACS Appl. Energ. Mater.* **2020**, *3*, 2935–2948.
[7] L. Gaines, Q. Dai, J. T. Vaughey, S. Gillard, *Recycling* **2021**, *6*, 31.
[8] T. Lombardo, M. Duquesnoy, H. El-Bouysidy, F. Årén, A. Gallo-Bueno, P. B. Jørgensen, A. Bhowmik, A. Demortière, E. Ayerbe, F. Alcaide, M. Reynaud, J. Carrasco, A. Grimaud, C. Zhang, T. Vegge, P. Johansson, A. A. Franco, *Chem. Rev.* **2022**, *122*, 10899–10969.
[9] E. Ayerbe, M. Berecibar, S. Clark, A. A. Franco, J. Ruhland, *Adv. Energy Mater.* **2021**, 12, 2102696.
[10] "DEFACTO project deliverable D2.1," can be found under https://defacto-project.eu/wp-content/uploads/2021/10/D2.1-Definition-of-Parameter-required-for-modelling_compressed.pdf, **2020**.
[11] "LiPlanet," can be found under https://www.liplanet.eu/, **n.d**.
[12] Y. Liu, R. Zhang, J. Wang, Y. Wang, *iScience* **2021**, *24*, 102332.
[13] W. B. Hawley, J. Li, *J. Energy Storage* **2019**, *25*, 100862.
[14] D. Liu, L.-C. Chen, T.-J. Liu, T. Fan, E.-Y. Tsou, C. Tiu, *Adv. Chem. Eng. Sci.* **2014**, *04*, 515–528.
[15] M. Haarmann, W. Haselrieder, A. Kwade, *Energy Technol.* **2020**, *8*, 1801169.
[16] T.-J. Liu, C. Tiu, L.-C. Chen, D. Liu, in *Print. Batter. Mater. Technol. Appl.* (Eds.: S. Lanceros-Méndez, C. Miguel Costa), John Wiley & Sons, Ltd, **2018**, pp. 63–79.
[17] H. Bockholt, M. Indrikova, A. Netz, F. Golks, A. Kwade, *J. Power Sources* **2016**, *325*, 140–151.
[18] F. Font, B. Protas, G. Richardson, J. M. Foster, *J. Power Sources* **2018**, *393*, 177–185.
[19] L. S. Kremer, A. Hoffmann, T. Danner, S. Hein, B. Prifling, D. Westhoff, C. Dreer, A. Latz, V. Schmidt, M. Wohlfahrt-Mehrens, *Energy Technol.* **2020**, *8*, 1–14.
[20] B. G. Westphal, A. Kwade, *J. Energy Storage* **2018**, *18*, 509–517.
[21] M. Luetke, V. Franke, A. Techel, T. Himmer, U. Klotzbach, A. Wetzig, E. Beyer, *Phys. Procedia* **2011**, *12*, 286–291.
[22] B. K. Antonopoulos, C. Stock, F. Maglia, H. E. Hoster, *Electrochim. Acta* **2018**, *269*, 331–339.
[23] S. J. An, J. Li, Z. Du, C. Daniel, D. L. Wood, *J. Power Sources* **2017**, *342*, 846–852.
[24] A. A. Franco, A. Rucci, D. Brandell, C. Frayret, M. Gaberscek, P. Jankowski, P. Johansson, *Chem. Rev.* **2019**, *119*, 4569–4627.
[25] A. A. Franco, *RSC Adv.* **2013**, *3*, 13027–13058.
[26] A. Mistry, A. A. Franco, S. J. Cooper, S. A. Roberts, V. Viswanathan, *ACS Energy Lett.* **2021**, *6*, 1422–1431.
[27] A. A. Franco, A. S. Barnard, *Batteries & Supercaps* **2022**, 5, e202200149.
[28] T. Lombardo, F. Caro, A. C. Ngandjong, J. Hoock, M. Duquesnoy, J. C. Delepine, A. Ponchelet, S. Doison, A. A. Franco, *Batteries & Supercaps* **2022**, 5, e202100324.
[29] T. Lombardo, F. Lambert, R. Russo, F. M. Zanotto, C. Frayret, G. Toussaint, P. Stevens, M. Becuwe, A. A. Franco, *Batteries & Supercaps* **2022**, e202200116.
[30] T. Lombardo, J. Hoock, E. N. Primo, A. C. Ngandjong, M. Duquesnoy, A. A. Franco, *Batteries & Supercaps* **2020**, *3*, 721–730.
[31] M. Duquesnoy, T. Lombardo, F. Caro, F. Haudiquez, A. C. Ngandjong, J. Xu, H. Oularbi, A. A. Franco, **2022**, arXiv preprint *arXiv:2201.04394*.
[32] C. Liu, O. Arcelus, T. Lombardo, H. Oularbi, A. A. Franco, *J. Power Sources* **2021**, *512*, 230486.
[33] R. P. Cunha, T. Lombardo, E. N. Primo, A. A. Franco, *Batteries & Supercaps* **2020**, *3*, 60–67.
[34] X. Ding, J. Liu, T. A. L. Harris, *AIChE J.* **2016**, *62*, 2508–2524.
[35] K. J. Ruschak, *Chem. Eng. Sci.* **1976**, *31*, 1057–1060.
[36] B. G. Higgins, L. E. Scriven, *Chem. Eng. Sci.* **1980**, *35*, 673–682.
[37] M. S. Carvalho, H. S. Kheshgi, *AIChE J.* **2000**, *46*, 1907–1917.
[38] O. J. Romero, L. E. Scriven, M. S. Carvalho, *J. Non-Newtonian Fluid Mech.* **2006**, *138*, 63–75.
[39] M. Duquesnoy, I. Boyano, L. Ganborena, P. Cereijo, E. Ayerbe, A. A. Franco, *Energy AI* **2021**, *5*, 100090.
[40] S. X. Drakopoulos, A. Gholamipour-Shirazi, P. MacDonald, R. C. Parini, C. D. Reynolds, D. L. Burnett, B. Pye, K. B. O'Regan, G. Wang, T. M. Whitehead, G. J. Conduit, A. Cazacu, E. Kendrick, *Cell Reports Phys. Sci.* **2021**, *2*, 100683.
[41] H. C. H. Rumpf, *Chem. Ing. Tech.* **1970**, *42*, 538–540.
[42] A. C. Ngandjong, A. Rucci, M. Maiza, G. Shukla, J. Vazquez-Arenas, A. A. Franco, *J. Phys. Chem. Lett.* **2017**, *8*, 5966–5972.
[43] A. Rucci, A. C. Ngandjong, E. N. Primo, M. Maiza, A. A. Franco, *Electrochim. Acta* **2019**, *312*, 168–178.
[44] M. Chouchane, A. Rucci, T. Lombardo, A. C. Ngandjong, A. A. Franco, *J. Power Sources* **2019**, *444*, 227285.
[45] T. Lombardo, A. C. Ngandjong, A. Belhcen, A. A. Franco, *Energy Storage Mater.* **2021**, *43*, 337–347.
[46] A. C. Ngandjong, T. Lombardo, E. N. Primo, M. Chouchane, A. Shodiev, O. Arcelus, A. A. Franco, *J. Power Sources* **2021**, *485*, 229320.
[47] M. Duquesnoy, T. Lombardo, M. Chouchane, E. N. Primo, A. A. Franco, *J. Power Sources* **2020**, *480*, 229103.
[48] C. Sangrós Giménez, B. Finke, C. Schilde, L. Froböse, A. Kwade, *Powder Technol.* **2019**, *349*, 1–11.
[49] C. Sangrós Giménez, C. Schilde, L. Froböse, S. Ivanov, A. Kwade, *Energy Technol.* **2020**, *8*, 1900180.
[50] X. Shan, H. Chen, *Phys. Rev. E* **1993**, *47*, 1815–1819.
[51] L. Chen, Q. Kang, Y. Mu, Y.-L. He, W.-Q. Tao, *Int. J. Heat Mass Transfer* **2014**, *76*, 210–236.
[52] A. Shodiev, E. Primo, O. Arcelus, M. Chouchane, M. Osenberg, A. Hilger, I. Manke, J. Li, A. A. Franco, *Energy Storage Mater.* **2021**, *38*, 80–92.
[53] A. Shodiev, M. Duquesnoy, O. Arcelus, M. Chouchane, J. Li, A. A. Franco, *J. Power Sources* **2021**, *511*, 230384.
[54] A. Nadeina, P. Rozier, V. Seznec, *Energy Technol.* **2020**, *8*, 1901304.

[55] A. Maurel, M. Armand, S. Grugeon, B. Fleutot, C. Davoisne, H. Tortajada, M. Courty, S. Panier, L. Dupont, *J. Electrochem. Soc.* **2020**, *167*, 070536.
[56] J. Hagemeister, F. J. Günter, T. Rinner, F. Zhu, A. Papst, R. Daub, *Submitted* **2022**.
[57] M. P. Lautenschlaeger, B. Prifling, B. Kellers, J. Weinmiller, T. Danner, V. Schmidt, A. Latz, *Batteries & Supercaps* **2022**, 5, e202200090.
[58] A. Shodiev, E. N. Primo, M. Chouchane, T. Lombardo, A. C. Ngandjong, A. Rucci, A. A. Franco, *J. Power Sources* **2020**, *454*, 227871.
[59] A. Shodiev, M. Chouchane, M. Gaberscek, O. Arcelus, J. Xu, H. Oularbi, J. Yu, J. Li, M. Morcrette, A. A. Franco, A. A. Fra, *Deconvoluting Benefits of Porosity Distribution in Layered Electrodes on Electrochemical Performance of Li-Ion Batteries*, Elsevier, **2022**.
[60] M. Chouchane, O. Arcelus, A. A. Franco, *Batteries & Supercaps* **2021**, *4*, 1457–1463.
[61] G. V. Silva, M. Thomitzek, T. Abraham, C. Herrmann, *Procedia CIRP* **2021**, *104*, 1017–1022.
[62] M. Weeber, J. Wanner, P. Schlegel, K. P. Birke, A. Sauer, *Procedia Manuf.* **2020**, *43*, 32–39.
[63] M. Vogt, C. Herrmann, *CIRP Ann.* **2021**, *70*, 21–24.
[64] S. Thiede, A. Turetskyy, T. Loellhoeffel, A. Kwade, S. Kara, C. Herrmann, *CIRP Ann.* **2020**, *69*, 21–24.
[65] M. Thomitzek, N. Von Drachenfels, F. Cerdas, C. Herrmann, S. Thiede, *Procedia CIRP* **2019**, *80*, 126–131.
[66] M. Schönemann, H. Bockholt, S. Thiede, A. Kwade, C. Herrmann, *Int. J. Adv. Manuf. Technol.* **2019**, *102*, 1373–1390.
[67] S. Ahmed, P. A. Nelson, K. G. Gallagher, D. W. Dees, *J. Power Sources* **2016**, *322*, 169–178.
[68] A. Jinasena, O. S. Burheim, A. H. Strømman, *Batteries* **2021**, *7*, 14.
[69] M. Vogt, A. Platzdasch, T. Abraham, C. Herrmann, *Procedia CIRP* **2022**, *105*, 410–415.
[70] A. Schilling, J. Schmitt, F. Dietrich, K. Dröder, *Energy Technol.* **2016**, *4*, 1502–1508.
[71] "ProZell – Das Projekt HoLiB stellt seine Forschungsinhalte vor.," can be found under https://prozell-cluster.de/projekte/holib/, **n.d**.
[72] J. Schmitt, A. Raatz, *Adv. Mater. Res.* **2014**, *907*, 309–319.
[73] A. Shodiev, F. M. Zanotto, J. Yu, M. Chouchane, J. Li, A. A. Franco, *Energy Storage Mater.* **2022**, *49*, 268–277.
[74] J. F. Jerier, B. Harthong, D. Imbault, F. V. Donzé, P. Dorémus, *AIP Conf. Proc.* **2009**, *1145*, 457.
[75] R. Tao, Z. Liang, S. Zhu, L. Yang, L. Ma, W. li Song, H. Chen, *Acta Mech. Solida Sin.* **2021**, *34*, 297–306.
[76] D. Lee, E. Kannatey-Asibu, W. Cai, *J. Manuf. Sci. Eng. Trans. ASME* **2013**, *135*, 061011 .
[77] A. P. Thompson, H. M. Aktulga, R. Berger, D. S. Bolintineanu, W. M. Brown, P. S. Crozier, P. J. in 't Veld, A. Kohlmeyer, S. G. Moore, T. D. Nguyen, R. Shan, M. J. Stevens, J. Tranchida, C. Trott, S. J. Plimpton, *Comput. Phys. Commun.* **2022**, *271*, 108171.
[78] C. Kloss, C. Goniva, A. Hager, S. Amberger, S. Pirker, *Prog. Comput. Fluid Dyn.* **2012**, *12*, 140–152.
[79] J. Latt, O. Malaspinas, D. Kontaxakis, A. Parmigiani, D. Lagrava, F. Brogi, M. Ben Belgacem, Y. Thorimbert, S. Leclaire, S. Li, F. Marson, J. Lemus, C. Kotsalos, R. Conradin, C. Coreixas, R. Petkantchin, F. Raynaud, J. Beny, B. Chopard, *Comput. Math. Appl.* **2021**, *81*, 334–350.
[80] J. Schnell, C. Nentwich, F. Endres, A. Kollenda, F. Distel, T. Knoche, G. Reinhart, *J. Power Sources* **2019**, *413*, 360–366.
[81] K. A. Severson, P. M. Attia, N. Jin, N. Perkins, B. Jiang, Z. Yang, M. H. Chen, M. Aykol, P. K. Herring, D. Fraggedakis, M. Z. Bazant, S. J. Harris, W. C. Chueh, R. D. Braatz, *Nat. Energy* **2019**, *4*, 383–391.
[82] K. Liu, X. Hu, H. Zhou, L. Tong, W. D. Widanage, J. Marco, *IEEE/ASME Trans. Mechatronics* **2021**, *26*, 2944–2955.
[83] A. Turetskyy, J. Wessel, C. Herrmann, S. Thiede, *Energy Storage Mater.* **2021**, *38*, 93–112.
[84] M. Vogt, K. Koch, A. Turetskyy, F. Cerdas, S. Thiede, C. Herrmann, *Procedia CIRP* **2021**, *98*, 157–162.
[85] M. F. Niri, K. Liu, G. Apachitei, L. A. A. Román-Ramírez, M. Lain, D. Widanage, J. Marco, *Energy AI* **2022**, *7*, 100129.
[86] K. Bockwinkel, C. Nowak, B. Thiede, M. Nöske, F. Dietrich, S. Thiede, W. Haselrieder, K. Dröder, A. Kwade, C. Herrmann, *Energy Technol.* **2020**, *8*, 1900133.
[87] T. Kornas, E. Knak, R. Daub, U. Bührer, C. Lienemann, H. Heimes, A. Kampker, S. Thiede, C. Herrmann, *Procedia CIRP* **2019**, *81*, 75–80.
[88] M. Kirchhof, K. Haas, T. Kornas, S. Thiede, M. Hirz, C. Herrmann, *Preprints* **2020**, 2020120312.
[89] O. Meyer, C. Weihs, S. Mähr, H. Y. Tran, M. Kirchhof, S. Schnackenberg, J. Neuhaus-Stern, S. Rößler, W. Braunwarth, *Energy Technol.* **2020**, *8*, 1900244.
[90] T. Komas, R. Daub, M. Z. Karamat, S. Thiede, C. Herrmann, *IEEE Int. Conf. Autom. Sci. Eng.* **2019**, *2019-August*, 380–385.
[91] M. Westermeier, G. Reinhart, M. Steber, *Procedia CIRP* **2014**, *20*, 13–19.
[92] K. Liu, Z. Wei, Z. Yang, K. Li, *J. Cleaner Prod.* **2021**, *289*, 125159.
[93] T. Chen, M. Song, H. Hui, H. Long, *Front. Energy Res.* **2021**, *9*, DOI: 10.3389/FENRG.2021.754317/FULL.
[94] O. Schmidt, M. Thomitzek, F. Röder, S. Thiede, C. Herrmann, U. Krewer, *J. Electrochem. Soc.* **2020**, *167*, 060501.
[95] J. R. Dean, *Practical Inductively Coupled Plasma Spectroscopy*, John Wiley & Sons, Ltd, **2005**, pp. 184.
[96] P. A. Tanguy, F. Thibault, C. Dubois, A. Aït-Kadi, *Chem. Eng. Res. Des.* **1999**, *77*, 318–324.
[97] G. Zhou, P. A. Tanguy, C. Dubois, *Chem. Eng. Res. Des.* **2000**, *78*, 445–453.
[98] A. Kraytsberg, Y. Ein-Eli, *Adv. Energy Mater.* **2016**, *6*, 1600655.
[99] W. B. Hawley, J. Li, *J. Energy Storage* **2019**, *26*, 100994.
[100] C. D. Reynolds, P. R. Slater, S. D. Hare, M. J. H. Simmons, E. Kendrick, *Mater. Des.* **2021**, *209*, 109971.
[101] S. H. Sung, D. H. Kim, S. Kim, M. H. Jeong, J. Nam, K. H. Ahn, *J. Mater. Sci.* **2019**, *54*, 13208–13220.
[102] W. J. Chang, G. H. Lee, Y. J. Cheon, J. T. Kim, S. Il Lee, J. Kim, M. Kim, W. Il Park, Y. J. Lee, *ACS Appl. Mater. Interfaces* **2019**, *11*, 41330–41337.
[103] W. B. Hawley, H. M. Meyer, J. Li, *Electrochim. Acta* **2021**, *380*, 138203.
[104] B. Zhao, Y. Gao, J. Ren, D. Yin, *J. Electron. Mater.* **2021**, *50*, 6818–6827.
[105] S. F. Kistler, P. M. Schweizer, *Liquid Film Coating: Scientific Principles and Their Technological Implications*, Chapman & Hall, London, Weinheim, New York, Tokyo, Melbourne, **1997**.
[106] E. D. Cohen, E. B. Gutoff, *Modern Coating and Drying Technology*, John Wiley & Sons, New York, **1992**.
[107] X. Li, C. Wang, *J. Mater. Chem. A* **2012**, *1*, 165–182.
[108] B. Ferrari, R. Moreno, L. Hernán, M. Melero, J. Morales, A. Caballero, *J. Eur. Ceram. Soc.* **2007**, *27*, 3823–3827.
[109] D. Gastol, M. Capener, C. Reynolds, C. Constable, E. Kendrick, *Mater. Des.* **2021**, *205*, 109720.
[110] J. Li, J. Fleetwood, W. B. Hawley, W. Kays, *Chem. Rev.* **2021**, acs.chemrev.1c00565.
[111] R. Diehm, H. Weinmann, J. Kumberg, M. Schmitt, J. Fleischer, P. Scharfer, W. Schabel, *Energy Technol.* **2020**, *8*, 1900137.
[112] L. Sartor, *Slot Coating: Fluid Mechanics and Die Design*, University of Minnesota, **1990**.
[113] O. J. Romero, W. J. Suszynski, L. E. Scriven, M. S. Carvalho, *J. Non-Newtonian Fluid Mech.* **2004**, *118*, 137–156.
[114] Y. S. Zhang, N. E. Courtier, Z. Zhang, K. Liu, J. J. Bailey, A. M. Boyce, G. Richardson, P. R. Shearing, E. Kendrick, D. J. L. Brett, *Adv. Energy Mater.* **2022**, *12*, 2102233.
[115] X. Wu, X. Li, X. Bei, *Mater. Sci. Forum* **2020**, *1003*, 260–267.
[116] N. Susarla, S. Ahmed, D. W. Dees, *J. Power Sources* **2018**, *378*, 660–670.
[117] M. Stein, A. Mistry, P. P. Mukherjee, *J. Electrochem. Soc.* **2017**, *164*, A1616–A1627.
[118] S. N. Bryntesen, A. H. Strømman, I. Tolstorebrov, P. R. Shearing, J. J. Lamb, O. Stokke Burheim, *Energies* **2021**, *14*, 1406.
[119] Z. Su, E. Decencière, T. T. Nguyen, K. El-Amiry, V. De Andrade, A. A. Franco, A. Demortière, *npj Comput. Mater.* **2022**, *8*, 1–11.
[120] S. Müller, C. Sauter, R. Shunmugasundaram, N. Wenzler, V. De Andrade, F. De Carlo, E. Konukoglu, V. Wood, *Nat. Commun.* **2021**, *12*, 1–12.
[121] H. Luo, J. Zhu, E. Sahraei, Y. Xia, *RSC Adv.* **2018**, *8*, 3996–4005.
[122] J. Vogel, *Theses Diss.* **2022**.
[123] L. A. Román-Ramírez, G. Apachitei, M. Faraji-Niri, M. Lain, W. D. Widanage, J. Marco, *J. Power Sources* **2021**, *516*, 230689.
[124] H. Hagiwara, W. J. Suszynski, L. F. Francis, *J. Coatings Technol. Res.* **2013**, *11*, 11–17.
[125] J. Kumberg, M. Baunach, J. C. Eser, A. Altvater, P. Scharfer, W. Schabel, *Energy Technol.* **2021**, *9*, 2000889.
[126] M. F. Niri, K. Liu, G. Apachitei, L. R. Ramirez, M. Lain, D. Widanage, J. Marco, *J. Cleaner Prod.* **2021**, *324*, 129272.
[127] C. Meyer, H. Bockholt, W. Haselrieder, A. Kwade, *J. Mater. Process. Technol.* **2017**, *249*, 172–178.
[128] X. Lu, S. R. Daemi, A. Bertei, M. D. R. Kok, K. B. O'Regan, L. Rasha, J. Park, G. Hinds, E. Kendrick, D. J. L. Brett, P. R. Shearing, *Joule* **2020**, *4*, 2746–2768.
[129] S. Malifarge, B. Delobel, C. Delacourt, *J. Electrochem. Soc.* **2017**, *164*, E3329–E3334.

[130] T. T. Nguyen, A. Demortière, B. Fleutot, B. Delobel, C. Delacourt, S. J. Cooper, *npj Comput. Mater.* **2020**, *6*, 1–12.
[131] C. Meyer, M. Weyhe, W. Haselrieder, A. Kwade, *Energy Technol.* **2020**, *8*, 1900175.
[132] C. Meyer, M. Kosfeld, W. Haselrieder, A. Kwade, *J. Energy Storage* **2018**, *18*, 371–379.
[133] A. Diener, S. Ivanov, W. Haselrieder, A. Kwade, *Energy Technol.* **2022**, *10*, 2101033.
[134] H. H. Heimes, A. Kampker, C. Lienemann, M. A. Locke, C. Offermanns, S. Michaelis, E. Rahimzei, *Produktionsprozess Einer Lithium-Ionen-Batteriezelle; 3. Auflage*, PEM Der RWTH Aachen Und VDMA Eigendruck, Frankfurt Am Main, **2018**.
[135] F. Huttner, W. Haselrieder, A. Kwade, *Energy Technol.* **2020**, *8*, 1900245.
[136] U. Langklotz, M. Schneider, A. Michaelis, *J. Ceram. Sci. Technol.* **2013**, *4*, 69–76.
[137] M. Kosfeld, B. Westphal, A. Kwade, *J. Energy Storage* **2022**, *51*, 104398.
[138] D. A. G. Bruggeman, *Ann. Phys.* **1935**, *416*, 636–664.
[139] D.-W. Chung, M. Ebner, D. R. Ely, V. Wood, R. Edwin García, *Model. Simul. Mater. Sci. Eng.* **2013**, *21*, 074009.
[140] T. Jansen, M. W. Kandula, S. Hartwig, L. Hoffmann, W. Haselrieder, K. Dilger, *Batteries* **2019**, *5*, 73.
[141] "Dew Point Transmitter DMT152 Dew point measurement in very dry environments | Vaisala," can be found under https://www.vaisala.com/en/products/instruments-sensors-and-other-measurement-devices/instruments-industrial-measurements/dmt152, **n.d**.
[142] "Analizador MB MO-SE1 | Manualzz," can be found under https://manualzz.com/doc/12962854/analizador-mb-mo-se1, **n.d**.
[143] "1511600 Analyzer MB-OX-SE1, 0–1000 ppm, 0–10 V // M. Braun Inertgas-Systeme GmbH," can be found under https://shop.mbraun.de/ENU/23348/Item.aspx?ItemNo=1511600, **n.d**.
[144] J. Canny, *IEEE Trans. Pattern Anal. Mach. Intell.* **1986**, *PAMI-8*, 679–698.
[145] R. O. Duda, P. E. Hart, *Commun. ACM* **1972**, *15*, 11–15.
[146] X. Chen, G. Shi, C. Xi, L. Zhong, X. Wei, K. Zhang, *J. Phys. Conf. Ser.* **2019**, *1237*, 032075.
[147] K. Wu, J. Tan, J. Li, C. Liu, *J. Phys. Conf. Ser.* **2021**, *1884*, 012024.
[148] O. Badmos, A. Kopp, T. Bernthaler, G. Schneider, *J. Intell. Manuf.* **2020**, *31*, 885–897.
[149] F. J. Günter, C. Burgstaller, F. Konwitschny, G. Reinhart, *J. Electrochem. Soc.* **2019**, *166*, A1709–A1714.
[150] W. J. Weydanz, H. Reisenweber, A. Gottschalk, M. Schulz, T. Knoche, G. Reinhart, M. Masuch, J. Franke, R. Gilles, *J. Power Sources* **2018**, *380*, 126–134.
[151] K. H. Pettinger, A. Kampker, C. R. Hohenthanner, C. Deutskens, H. Heimes, A. vom Hemdt, in *Lithium-Ion Batteries: Basics and Applications* (Eds.: R. Korthauer), Springer, Berlin, Heidelberg, **2018**, pp. 211–226.
[152] Y. Morizane, *Method for Electrolyte Injection*, **2002**, US6497976B1.
[153] F. J. Günter, J. Keilhofer, C. Rauch, S. Rössler, M. Schulz, W. Braunwarth, R. Gilles, R. Daub, G. Reinhart, *J. Power Sources* **2022**, *517*, 230668.
[154] A. Davoodabadi, J. Li, H. Zhou, D. L. Wood, T. J. Singler, C. Jin, *J. Energy Storage* **2019**, *26*, 101034.
[155] Y. Sheng, C. R. Fell, Y. K. Son, B. M. Metz, J. Jiang, B. C. Church, *Front. Energy Res.* **2014**, *2*, 56.
[156] A. Schilling, S. Wiemers-Meyer, V. Winkler, S. Nowak, B. Hoppe, H. H. Heimes, K. Dröder, M. Winter, *Energy Technol.* **2020**, *8*, 1900078.
[157] S. Beyer, O. Kobsch, D. Pospiech, F. Simon, C. Peter, K. Nikolowski, M. Wolter, B. Voit, *J. Adhes. Sci. Technol.*. **2019**, *34*, 849–866.
[158] Y. Suharto, Y. Lee, J. S. Yu, W. Choi, K. J. Kim, *J. Power Sources* **2018**, *376*, 184–190.
[159] M. Liu, P. Zhang, L. Gou, Z. Hou, B. Huang, *Mater. Lett.* **2017**, *208*, 98–101.
[160] N. Kaden, N. Schlüter, R. Leithoff, S. Savas, S. Grundmeier, K. Dröder, *Process.* **2021**, *9*, 1851.
[161] T. Knoche, V. Zinth, M. Schulz, J. Schnell, R. Gilles, G. Reinhart, *J. Power Sources* **2016**, *331*, 267–276.
[162] F. J. Günter, J. B. Habedank, D. Schreiner, T. Neuwirth, R. Gilles, G. Reinhart, *J. Electrochem. Soc.* **2018**, *165*, A3249–A3256.
[163] Z. Deng, Z. Huang, Y. Shen, Y. Huang, H. Ding, A. Luscombe, M. Johnson, J. E. Harlow, R. Gauthier, J. R. Dahn, *Joule* **2020**, *4*, 2017–2029.
[164] S. G. Lee, D. H. Jeon, *J. Power Sources* **2014**, *265*, 363–369.
[165] Z. Guo, Y. Fan, *RSC Adv.* **2016**, *6*, 8971–8979.
[166] K. Kohno, Y. Koishikawa, Y. Yagi, T. Horiba, *J. Power Sources* **2008**, *185*, 554–558.
[167] 郑丁, 张兴国, 董峰, 史离全, 张景国, 吴赛舟, 王亚超, *Method for Controlling Heat Sealing Quality of Aluminum Plastic Film Soft Package Battery*, **2012**, CN103424227 A.
[168] K. H. Lee, E. H. Song, J. Y. Lee, B. H. Jung, H. S. Lim, *J. Power Sources* **2004**, *132*, 201–205.
[169] W. Song, J. Harlow, E. Logan, H. Hebecker, M. Coon, L. Molino, M. Johnson, J. Dahn, M. Metzger, *J. Electrochem. Soc.* **2021**, *168*, 090503.
[170] C. P. Aiken, J. Xia, D. Y. Wang, D. A. Stevens, S. Trussler, J. R. Dahn, *J. Electrochem. Soc.* **2014**, *161*, A1548–A1554.
[171] B. Rowden, N. Garcia-Araez, *Energy Reports* **2020**, *6*, 10–18.
[172] J.-P. Schmiegel, M. Leißing, F. Weddeling, F. Horsthemke, J. Reiter, Q. Fan, S. Nowak, M. Winter, T. Placke, *J. Electrochem. Soc.* **2020**, *167*, 060516.
[173] J. Flórez-Montaño, G. García, O. Guillén-Villafuerte, J. L. Rodríguez, G. A. Planes, E. Pastor, *Electrochim. Acta* **2016**, *209*, 121–131.
[174] N. A. Z. R-Smith, M. Ragulskis, M. Kasper, S. Wagner, J. Pumsleitner, B. Zollo, A. Groebmeyer, F. Kienberger, *IEEE Trans. Instrum. Meas.* **2021**, *70*, DOI: 10.1109/TIM.2021.3100331.
[175] S. M. Lambert, M. Armstrong, P. S. Attidekou, P. A. Christensen, J. D. Widmer, C. Wang, K. Scott, *IEEE Trans. Ind. Electron.* **2017**, *64*, 4017–4026.
[176] S. Das, P. M. Attia, W. C. Chueh, M. Z. Bazant, *J. Electrochem. Soc.* **2019**, *166*, E107–E118.
[177] D. Witt, F. Röder, U. Krewer, *Batteries & Supercaps* **2022**, DOI: 10.1002/batt.202200067.
[178] F. Röder, R. D. Braatz, U. Krewer, *J. Electrochem. Soc.* **2017**, *164*, E3335–E3344.
[179] F. Röder, R. D. Braatz, U. Krewer, *Comput. Aided Chem. Eng.* **2016**, *38*, 157–162.
[180] D. Diddens, W. A. Appiah, Y. Mabrouk, A. Heuer, T. Vegge, A. Bhowmik, D. Diddens, Y. Mabrouk, A. Heuer, W. A. Appiah, T. Vegge, A. Bhowmik, *Adv. Mater. Interfaces* **2022**, *9*, 2101734.
[181] A. Turetskyy, S. Thiede, M. Thomitzek, N. von Drachenfels, T. Pape, C. Herrmann, *Energy Technol.* **2020**, *8*, 1900136.
[182] J. Wessel, A. Turetskyy, O. Wojahn, C. Herrmann, S. Thiede, *Procedia CIRP* **2020**, *93*, 162–167.
[183] B. ISO 9000, *London Br. Stand. Inst.* **2000**.
[184] J. Ryu, D. Taillard, C. Janssen, *GS1 Global Traceability Standard* **2017**.
[185] T. Moe, *Trends Food Sci. Technol.* **1998**, *9*, 211–214.
[186] G. Riexinger, J. P. Doppler, C. Haar, M. Trierweiler, A. Buss, K. Schöbel, D. Ensling, T. Bauernhansl, *Procedia CIRP* **2020**, *93*, 125–130.
[187] A. Sommer, M. Leeb, S. Haghi, F. J. Günter, G. Reinhart, *Procedia CIRP* **2021**, *104*, 1011–1016.
[188] J. Wessel, A. Turetskyy, O. Wojahn, T. Abraham, C. Herrmann, *Procedia CIRP* **2021**, *104*, 1215–1220.
[189] "OpenSemanticLab·GitHub," can be found under https://github.com/OpenSemanticLab, **n.d**.
[190] "KIproBatt Wiki," can be found under https://kiprobatt.de/wiki/Main_Page, **n.d**.
[191] "BIG-MAP Project," can be found under https://www.big-map.eu/, **n.d**.
[192] S. Clark, F. L. Bleken, S. Stier, E. Flores, C. W. Andersen, M. Marcinek, A. Szczesna-Chrzan, M. Gaberscek, M. R. Palacin, M. Uhrin, J. Friis, *Adv. Energy Mater.* **2021**, 2102702.
[193] "(PDF) Towards a comprehensive semantic information structure in the battery value chain," can be found under https://www.researchgate.net/publication/355843865_Towards_a_comprehensive_semantic_information_structure_in_the_battery_value_chain?channel=doi&linkId=6180ea78a767a03c14e24307&showFulltext=true, **n.d**.
[194] "GitHub – General-Process-Ontology/ontology," can be found under https://github.com/General-Process-Ontology/ontology, **n.d**.
[195] "Battery-Value-Chain-Ontology·GitHub," can be found under https://github.com/Battery-Value-Chain-Ontology, **n.d**.
[196] A. A. Franco, "ARTISTIC Computational portal," can be found under https://www.erc-artistic.eu/computational-portal, **n.d**.
[197] F. Duffner, N. Kronemeyer, J. Tübke, J. Leker, M. Winter, R. Schmuch, *Nat. Energy* **2021**, *6*, 123–134.
[198] O. Arcelus, A. A. Franco, *J. Phys. Energy* **2022**, *4*, 011002.
[199] F. Rahmanian, J. Flowers, D. Guevarra, M. Richter, M. Fichtner, P. Donnely, J. M. Gregoire, H. S. Stein, *Adv. Mater. Interfaces* **2022**, 9, 2101987.
[200] L. M. Roch, F. Häse, C. Kreisbeck, T. Tamayo-Mendoza, L. P. E. Yunker, J. E. Hein, A. Aspuru-Guzik, *Sci. Robot.* **2018**, *3*, DOI: 10.1126/SCIROBOTICS.AAT5559.

Manuscript received: May 17, 2022
Revised manuscript received: July 7, 2022
Accepted manuscript online: July 19, 2022
Version of record online: August 9, 2022